

Agentic AI – Physicist Collaboration in Experimental Particle Physics: A Proof-of-Concept Measurement with LEP Open Data

Anthony Badea^a Yi Chen^b Yen-Jie Lee^c

^a *University of Chicago, Enrico Fermi Institute, 60637 IL, USA*

^b *Vanderbilt University, Nashville, Tennessee, USA*

^c *Laboratory for Nuclear Science, Massachusetts Institute of Technology, Cambridge, MA 02139, USA*

E-mail: anthony.badea@cern.ch

ABSTRACT: We present an AI agentic measurement of the thrust distribution in e^+e^- collisions at $\sqrt{s} = 91.2$ GeV using archived ALEPH data. The analysis and all note writing is carried out entirely by AI agents (OpenAI Codex and Anthropic Claude) under expert physicist direction. A fully corrected spectrum is obtained via Iterative Bayesian Unfolding and Monte Carlo based corrections. This work represents a step toward a theory–experiment loop in which AI agents assist with experimental measurements and theoretical calculations, and synthesize insights by comparing the results, thereby accelerating the cycle that drives discovery in fundamental physics. Our work suggests that precision physics, leveraging the open LEP data and advanced theoretical landscape, provides an ideal testing ground for developing advanced AI systems for scientific applications.

KEYWORDS: QCD, event shapes, electron-positron collisions, unfolding, artificial intelligence, large language models

Contents

1	Context of e^+e^- Alliance	1
2	Introduction	3
3	AI-agent usage in this analysis program	5
3.1	Scope and operating model	5
3.2	Inputs and context supplied to agents	6
3.3	Boundaries, controls, and reproducibility	6
3.4	Why this matters for the broader physics program	7
4	ALEPH detector	8
5	Data and simulated event samples	9
6	Event reconstruction and selection	10
6.1	Particle categories and <code>pwflag</code> mapping	10
6.2	Object-level and event-level selections	11
6.3	Particle-category kinematic validation	12
6.4	Event-level selection observables	20
7	Analysis method	22
7.1	Observable definition and nominal configuration	22
7.2	Response construction from matched MC	22
7.3	Iterative Bayesian Unfolding setup and iteration choice	23
7.4	Thrust resolution study	24
7.5	Systematics execution map	25
7.6	Hadronic correction, ISR correction, covariance propagation, and matrix exports	25
8	Systematic uncertainties	26
8.1	Statistical uncertainty	27
8.2	Experimental systematic uncertainties	28
8.3	Theory systematic uncertainties	31
8.4	Hadronic event-selection correction	32
8.5	ISR correction	33
8.6	Statistical covariance	33
8.7	Combination model	34
8.8	Uncertainty breakdown	34

9	Results	35
9.1	Final unfolded thrust distribution	35
9.2	Per-source correlation matrices	41
9.3	Per-source covariance matrices	42
10	Conclusion	44
11	Challenges with AI-agent analysis	45
11.1	Current limitations of the thrust-only baseline	45
11.2	Persistent analysis challenges	45
11.3	Update protocol for this section	46
11.4	Scaling human oversight: toward systematic validation	46
A	Workflow code and reproduction contract	49
A.1	Executable workflow map	49
A.2	Reproduction contract	50
A.3	Workflow pseudocode	50
B	Validation and cross-check details	51
B.1	Iteration-scan closure and stability	51
B.2	OmniFold and prior IBU comparison	51
B.3	Difference-check program	52
B.4	Output integrity verification	52
C	Communication summary (reconstructed project-cycle transcript)	52
C.1	Scope and reconstruction sources	52
C.2	Reconstructed communication timeline	52
C.3	Key exchanges and decisions	54
C.4	Communication-pattern summary	55

1 Context of e^+e^- Alliance

Achieving Standard Model predictions at the level of precision required for future collider programs, including the High-Luminosity Large Hadron Collider (HL-LHC), is essential to ensure robust control of systematic uncertainties in the interpretation of potential new physics anomalies. The demand for such precision is driven by percent-level experimental uncertainties and the unprecedented statistical power of modern collider datasets. In this regime, theoretical uncertainties become limiting, and the dominant contribution arises from our modeling of Quantum Chromodynamics, often referred to as precision QCD.

Precision QCD studies can be pursued at hadron colliders such as the LHC, but they are most cleanly and systematically tested in lepton collider environments. At present, however, there is no active high-energy lepton collider operating at LEP energies or above.

To address this, the e^+e^- alliance [1] has successfully curated and reanalyzed archived datasets from the Large Electron–Positron collider (LEP), the precursor to the LHC, opening new opportunities enabled by three decades of theoretical advances and modern experimental techniques. The combination of ultra-precise e^+e^- data and state-of-the-art perturbative and non-perturbative QCD tools provides a uniquely powerful environment for high-precision studies. The alliance has produced a series of precision measurements using these archived datasets, including two-particle correlations [2], jet energy spectra and substructure [3], long-range near-side correlations [4], energy-energy correlators [5], and unbinned measurements of thrust [6].

More broadly, this program is a compelling opportunity for AI for Science in a domain where precision is paramount. While AI is increasingly used to assist theoretical calculations and generate predictions, in the physical sciences such predictions ultimately require experimental validation. In high-energy physics, this validation depends on collider datasets that are rarely publicly accessible. The e^+e^- environment, particularly at LEP energies, provides the cleanest setting for precision tests of QED and QCD, with well-defined initial states and calculable dynamics. The successful curation and use of archived open data therefore establishes the conditions for a theory–experiment loop in which AI systems, guided by domain experts, can propose new calculations, observables, or improved models and directly confront them with high-precision data. This creates a concrete framework for developing AI systems that do not merely interpolate existing knowledge, but actively refine theoretical descriptions through direct comparison with experiment.

Lessons from AI–Physicist Collaboration

Carrying out this analysis has also produced practical insights into how AI agents and physicists can work together effectively. Our workflow followed a constrained human-in-the-loop cycle in which the physicist defined physics objectives, acceptance criteria, and interpretation authority, while the AI agent owned implementation throughput, consistency checks, and traceability. Crucially, experienced physicists also contributed domain intuition that cannot be reduced to formal specifications alone, including judgments about physically meaningful binning, acceptable regularization behavior, uncertainty communication, and when apparent anomalies warranted deeper investigation. Requests were made concrete and executable, each iteration linked to specific scripts, outputs, and note sections, and corrections were applied incrementally and revalidated rather than batched into large unreviewed changes.

From this experience, several recurring challenge classes emerged. Implicit physics priors, expert expectations about acceptable binning, regularization behavior, or uncertainty presentation, were often assumed rather than explicitly stated, requiring iterative clarification. Precision formatting constraints (label offsets, legend placement, pad geometry) required many short feedback loops, and apparent cosmetic changes sometimes affected interpretability and therefore physics conclusions. State synchronization across rapidly evolving scripts, outputs, and note text demanded continuous provenance refreshing. Throughout, authority remained intentionally asymmetric: the physicist owns physics choices and release signoff, while the agent executes and refactors. These lessons motivate

stricter templating for figures, stronger configuration contracts, and clearer channels for encoding expert heuristics into machine readable constraints in future iterations of this program.

2 Introduction

Machine learning has been central to high-energy physics for decades, enabling reconstruction algorithms, event classification, and detector optimization across collider experiments. A new frontier has emerged with large language models (LLMs) developed by major AI laboratories, including Anthropic [7], OpenAI [8], Google DeepMind [9], and others, that can now assist directly with scientific reasoning, mathematical proof, and code generation. A striking asymmetry persists: AI has transformed the theoretical and computational side of fundamental physics research—assisting derivations of new results in theoretical particle physics [10], designing novel protein structures for biology and health research [11], and simplifying complex calculations. Yet the experimental side of the AI-assisted research loop remains largely absent. To realize a future where AI rapidly accelerates the discovery of new physics, AI-assisted scientific workflows must be developed and validated across *both* precision theory *and* precision experiment.

A logical first step toward closing this gap is an agentic analysis of real experimental data with expert physicist oversight. This is precisely the approach pursued here: the physicist opened AI Agent (OpenAI Codex and Anthropic Claude Code), brainstormed the analysis goals, then iteratively prompted the AI agents to execute the full analysis workflow. No analysis code was written by hand; the physicist’s role is analogous to advising a graduate student, providing expert direction, reviewing results, and iterating. The agent was supplied with context comprising the published ALEPH thrust paper [12], prior ROOT-based ALEPH analysis macros covering event selection and thrust calculation, internal analysis notes documenting the miniDST data format and detector calibration procedures, and the LEP open-data files themselves. No pre-written unfolding or systematic-uncertainty code was provided; instead, the physicist described the physics objectives and acceptance criteria in iterative prompts, and the agent constructed the corresponding implementations from those descriptions. This prompting strategy follows from the established understanding in the AI literature that few-shot examples and supplied context improve AI-assisted outputs [13, 14]. A detailed inventory of the inputs and prompting approach is given in Sec. 3. Pursuing this theory–experimental interface for physics will inevitably deepen understanding of AI capabilities and their potential to improve AI systems for science domains where precision matters.

This vision parallels the evolution of AI in neighboring scientific domains. In materials science and structural biology, AI work has progressed from computational prediction with post-hoc human validation toward AI-designed experiments executed by autonomous robotic systems, creating closed feedback loops where AI proposes, executes, measures, and learns. High-energy physics faces a parallel opportunity. While we cannot deploy robotic particle detectors (yet), the emergence of open, curated data, partially enabled by the e^+e^- alliance [1], from past experiments, particularly the precision LEP dataset, can serve as

a “pseudo-laboratory” for developing and validating AI-assisted scientific workflows that operate across the precision theory–experiment interface [2, 3]. This requires infrastructure on both sides: precise theoretical predictions and experimental measurements with rigorous uncertainty quantification, where AI-assisted reasoning is tested and held accountable to measurable constraints [15–17].

Precision QCD provides an excellent domain for this program, precisely because of the combination of high-precision e^+e^- data and sophisticated high-precision theory calculations. Achieving Standard Model predictions at the precision required for future collider programs, including the High-Luminosity LHC, demands QCD calculations with uncertainty control matched to percent-level experimental precision. In this regime, precision experimental measurement becomes validation infrastructure for AI models. When percent-level uncertainties are coupled to rigorous covariance quantification and end-to-end reproducibility, high-precision measurements define the testing ground where AI predictions are made quantitative, falsifiable, and subject to rigorous scientific accountability. Although there is currently no active high-energy lepton collider operating at LEP energies or above—while lower-energy e^+e^- colliders such as BEPCII operate at $\sqrt{s} \lesssim 5$ GeV—archived LEP data now provide an unprecedented open-data opportunity for precision studies with excellent uncertainty control [1–3]. Relative to hadron- and nuclear-collision open-data settings, the LEP e^+e^- environment is considerably simpler experimentally and theoretically, making it a uniquely clean testing ground for new research in precision Physics+AI development.

From both an AI and precision physics perspective, thrust is an ideal first variable for this program. Thrust probes both perturbative radiation and non-perturbative dynamics in a single distribution, is computable at high perturbative order, and has well-established connections to resummed calculations, making comparison to theory controlled and interpretable [12, 18, 19]. Thrust, along with other event-shape observables measured at LEP, continue to anchor comparisons between perturbative calculations, generator modeling, and non-perturbative hadronization constraints. Recent thrust-based α_s extractions report $\alpha_s(m_Z) \simeq 0.1136 \pm 0.0012$, below the 2023 world-average value $\alpha_s(m_Z) = 0.1180 \pm 0.0009$ [20, 21]. This persistent tension, often referred to as the e^+e^- α_s puzzle, is of great interest because α_s is the least precisely measured fundamental constant of nature. The associated uncertainties propagate to all measurements involving QCD, and the effective field theory tools used to extract α_s are widely employed throughout the field. Put differently, if something is missed in the simplest case of e^+e^- collisions, it is likely that similar effects will also be missed in precision studies of more complex systems such as pp collisions.

The immediate objective of this note is to establish a robust detector-corrected thrust baseline using Iterative Bayesian Unfolding (IBU) implemented in RooUnfold, with complete validation and systematic propagation. The agent was asked to execute the full analysis loop: data and simulation processing, unfolding orchestration, systematic propagation, figure production, and note maintenance with traceable links to code and outputs. This analysis is also part of a broader program of AI-assisted scientific workflows in high-energy physics, where agent-oriented frameworks are developing rapidly alongside

AI-assisted theoretical calculations [17, 22–28]. We utilize the thrust measurement as a testing ground to understand the capabilities of the agent, establish a software base to conduct agentic analysis of the LEP data, and identify areas for improvement. We note that areas for improvement include both the core capabilities of the AI and the interaction of the physicist with the AI. In addition to the unfolded spectrum, complete covariance and correlation matrices are produced for downstream phenomenology use. We envision using our work to pursue a next stage, where the same framework will be extended to additional event-shape observables (C-parameter and heavy-jet mass), and the approach of using AI-assisted scientific workflows for both theoretical and experimental analysis will be pursued in a loop between them. Since thrust is computed from selected charged and neutral particles, the note also includes detailed `pwflag`-resolved kinematic comparisons between data and simulation before the unfolding stage.

The remainder of the document is structured as follows: Sec. 1 provides context of the e^+e^- alliance program, including lessons from AI–physicist collaboration; Sec. 3 defines the AI-agent operating model used in this internal analysis cycle; Sec. 4 summarizes detector elements most relevant for event-shape reconstruction; Sec. 5 describes data and simulation samples; Sec. 6 details reconstruction and selections, including particle-category and event-level validation; Sec. 7 presents thrust construction and the executable unfolding workflow; Sec. 8 and Sec. 9 document uncertainty propagation and the final thrust baseline outputs; Sec. 10 reports our conclusions from the study; Sec. 11 closes the note with persistent analysis challenges and mitigation tracking.

3 AI-agent usage in this analysis program

This internal note includes an explicit evaluation of AI-agent support for an experimental QCD analysis workflow. The central question is not only whether an agent can generate text or isolated scripts, but whether it can execute a full analysis loop under physicist supervision: data and MC processing, unfolding orchestration, systematic propagation, figure production, and note maintenance with traceable links to code and outputs.

3.1 Scope and operating model

The agent used in this analysis is interfaced through Anthropic Claude Code and OpenAI Codex, depending on the preference of the physicist. The operating model is human-in-the-loop: the physicist formulates goals and provides expert direction through iterative prompts; the agent executes the corresponding implementation steps; the physicist reviews the outputs and provides feedback; the process is then repeated. Physics decisions remain analyst-owned, while the agent provides implementation speed, consistency checks, and documentation rigor. In practical terms, the agent is used to:

- execute and monitor multi-step workflows;
- enforce consistent plotting and note formatting conventions;
- connect analysis statements in the note to concrete script paths, configuration keys, and produced artifacts;

- iterate quickly on uncertainty-view and validation presentation.

This model is intentionally conservative: the agent is treated as an accelerator for engineering and documentation tasks, not as an autonomous scientific decision-maker at this stage. The interaction is analogous to advising a graduate student, where the physicist supplies expert judgment and direction while the student (agent) carries out the technical execution.

3.2 Inputs and context supplied to agents

The context supplied to the agent at the start of each session can be grouped into four categories. First, *reference materials*: the published ALEPH thrust measurement [12], prior ROOT-based analysis macros for event selection and thrust calculation, and internal analysis notes documenting the miniDST format, detector calibration, and `pwflag` definitions. Second, *data inputs*: the LEP 1 open-data miniDST files for the 1994 running period at $\sqrt{s} = 91.2$ GeV, together with the corresponding ALEPH Monte Carlo simulation samples. Third, *physicist-written prompts*: each iteration began with a prompt specifying the physics objective (e.g. “propagate the hadronic-event correction as an independent systematic component with per-bin envelope uncertainties”), acceptance criteria (e.g. “refolded spectra must reproduce detector-level data within statistical precision”), and output-format expectations (figure style, table layout, note section to update). Fourth, *what was not supplied*: no pre-written unfolding code, no systematic-uncertainty framework, and no covariance-matrix infrastructure were provided. The agent constructed these from the physics descriptions in the prompts, using the reference code as stylistic guidance rather than as a template to copy. This distinction is important for assessing what the agent can build from first principles versus what it merely adapts from existing implementations.

3.3 Boundaries, controls, and reproducibility

To keep scientific accountability explicit, each high-impact step has a control point where analyst sign-off is required before results are treated as baseline:

- event and object selection definition;
- nominal unfolding regularization choice;
- systematic-combination policy;
- final figure and uncertainty-presentation choices;
- interpretation language in the note.

Beyond these sign-off gates, the physicist performed concrete validation checks at each major analysis stage. These checks are enumerated here to make the human-oversight component explicit and reproducible.

Event selection. Cut-flow yields were compared to the published ALEPH numbers [12] to verify selection efficiency. Distributions of $\cos \theta_{\text{thrust}}$ and φ were inspected for detector

artifacts; this step uncovered a localized φ excess in the data that was traced to a detector region and corrected before proceeding.

Unfolding. Refolded spectra were required to reproduce the detector-level data within statistical precision. An iteration scan confirmed that χ^2/ndf is stable across iterations 4–6. Independent cross-checks with OmniFold ($\chi^2/\text{ndf} = 0.663$) and a prior-sensitivity IBU variant ($\chi^2/\text{ndf} = 0.421$) were reviewed to ensure the baseline result is not an artifact of the nominal method.

Systematic uncertainties. Each variation’s impact on the unfolded distribution was inspected for bin-to-bin continuity and physical reasonableness. The total covariance matrix was verified to be positive semi-definite. The $\sim 23\%$ difference between energy-flow and charged-only thrust was confirmed to be an observable-redefinition effect rather than a detector systematic (see Sec. 8.2).

Final result. The unfolded thrust distribution was compared to the ALEPH 2004 published result, yielding $\chi^2/\text{ndf} = 0.36$ over 42 bins. Per-bin uncertainty breakdowns were examined for pathological bins, particularly the endpoint region $T \in [0.99, 1.00]$.

Documentation. All figure captions, table entries, and interpretive statements in the note were reviewed by the physicist for physics accuracy. Agent-generated text was treated as a draft requiring human approval before inclusion in the baseline.

Reproducibility is ensured through multiple complementary mechanisms. All analysis steps are version-controlled, with code and configuration managed in a git repository so that any result can be traced to a specific commit and set of inputs. Workflow runs produce structured output artifacts, including summary files that capture the configuration used, the software versions, and checksums of key outputs. Physicist oversight at each review stage provides an additional layer of validation: discrepancies between expected and observed outputs are flagged before any result is promoted to the baseline. These controls together ensure that results are reproducible independently of the AI agent’s involvement and that the physicist retains full accountability for all scientific claims.

3.4 Why this matters for the broader physics program

The broader objective of this work is to extend modern AI, including large language models (LLMs), beyond purely theoretical calculations in fundamental physics. To fully close the theory–experiment loop, the experimental side must produce reliable, uncertainty-aware observables and covariance products that can be directly consumed by precision QCD fits. In this vision, AI is applied not only to theoretical calculations but also to experimental analysis workflows.

The goal is to accelerate progress in fundamental physics by leveraging AI agents, LLMs, and other advanced models across both domains, ideally within a feedback loop between theory and experiment. In this loop, theory predictions inform experimental analyses, whose results in turn constrain and guide further theoretical proposals. Throughout this process, the physicist provides expert oversight and validation at each stage.

Recent case studies in AI-assisted scientific discovery and HEP theory support this direction, while also emphasizing verification, reproducibility, and expert oversight as essential constraints for reliable deployment of such systems [17, 26–28]. In the present work,

the experimental–theory bridge is represented by release-grade covariance and correlation outputs for thrust, with the next step being an expansion to additional event-shape observables such as the C-parameter and heavy-jet mass, and ultimately to multidimensional constraints.

This section therefore serves both as a methodological statement and as a proof of concept. In particular, it shows that an AI agent can assist with end-to-end execution of experimental workflows when constrained by explicit controls, validation checks, and human review. The operational details of this collaboration model, including the interaction protocol and persistent bottlenecks observed from the agent perspective, are documented in Sec. 11.

4 ALEPH detector

ALEPH was a general-purpose LEP detector with near 4π coverage and high-precision charged-particle tracking in a 1.5 T solenoidal magnetic field [29, 30]. The detector subsystems most relevant for this event-shape analysis are the central tracker, electromagnetic and hadronic calorimeters, and outer muon chambers.

The central tracking system combined a silicon vertex detector (VDET), an inner tracking chamber (ITC), and a large time projection chamber (TPC) with 21 pad rows covering $|\cos\theta| < 0.97$. Together these detectors provided precise track parameters and momentum measurements, and they define the object-quality observables used in this analysis (for example d_0 , z_0 , and N_{TPC}). The single-track momentum resolution achieved by the combined tracking system is $\sigma(1/p_T) \simeq 6 \times 10^{-4} \text{ GeV}^{-1}$.

The calorimeter system comprised two main subsystems. The electromagnetic calorimeter (ECAL) achieved an energy resolution of $\sigma_E/E \simeq 0.18/\sqrt{E [\text{GeV}]}$, providing the primary response to photons and electromagnetic showers and anchoring the neutral-energy scale for event-shape reconstruction. The hadronic calorimeter (HCAL) with resolution $\sigma_E/E \simeq 0.85/\sqrt{E [\text{GeV}]}$ is essential for neutral-hadron energy flow and global visible-energy reconstruction. The muon system outside HCAL supports lepton categorization in the archived ALEPH object definitions.

A key feature of the ALEPH reconstruction is the energy-flow algorithm, which combines tracking and calorimetric information to form a set of energy-flow objects that represent both charged and neutral particle candidates in the event. Tracking information dominates for charged particles, where the momentum resolution is superior to the calorimeter energy resolution. Calorimetric information provides the primary input for neutral particles (photons and neutral hadrons), which leave no track in the TPC. The combined energy-flow reconstruction achieves an energy resolution of $\sigma(E) = (0.59 \pm 0.03)\sqrt{E/\text{GeV}} + (0.6 \pm 0.3) \text{ GeV}$ for hadronic events [12]. This energy-flow approach, used in the ALEPH 2004 published event-shape analysis [12], is the particle-level input adopted for the present analysis. The 1998 ALEPH event-shape analysis [31] used charged particles only to minimize model dependence on neutral-energy simulation; our nominal analysis follows the 2004 approach using both charged and neutral energy-flow objects, with a charged-only variation retained as a cross-check.

In this analysis, we use the archived ALEPH reconstructed object representation directly, including per-particle category labels (`pwflag`) and kinematic variables. Event-shape observables are built from selected charged and neutral energy-flow objects, so detector performance in each reconstructed particle category is a direct input to thrust migration and unfolding stability.

5 Data and simulated event samples

The nominal measurement uses archived ALEPH LEP1 data from 1994 at $\sqrt{s} \simeq 91.2$ GeV. This period is used because matched detector-level and generator-level archived MC inputs required for unfolding are available in this configuration. The 1994 sample corresponds to approximately 40 pb^{-1} after quality requirements, yielding approximately 1.33 million selected hadronic events, and provides the largest fully synchronized archived data/MC configuration for this workflow.

Detector corrections are derived from archived ALEPH MC processed through the same analysis chain. The archived MC was produced with the standard ALEPH detector simulation software chain (JETSET 7.4 parton shower and hadronization with the ALEPH tune, GEANT 3 detector simulation), consistent with the simulation used in the published ALEPH event-shape analyses of the same dataset [12]. In the preserved sample, the detector-level and generator-level event records are connected through a common event identifier, enabling event-matched response construction and post-unfolding hadronic-selection corrections.

The unfolded result is corrected to stable-hadron level, defined as all final-state particles with stable or long-lived decays, inclusive over the full hadronic Z phase space. Two generator-level corrections are applied after unfolding.

The hadronic event-selection correction,

$$C_{\text{had}}(j) = \frac{N_{\text{genBefore}}(j)}{N_{\text{gen}}(j)}, \quad (5.1)$$

accounts for the efficiency of the hadronic event selection at the generator level: multiplying the unfolded spectrum by C_{had} restores events lost to the hadronic selection, yielding a result independent of the generator-level hadronic event selection.

An initial-state radiation (ISR) correction,

$$C_{\text{ISR}}(j) = \frac{N_{\text{noISR}}^{\text{gen}}(j)}{N_{\text{ISR}}^{\text{gen}}(j)}, \quad (5.2)$$

would additionally correct the result from the ISR-inclusive generator-level distribution to the pure $\sqrt{s} = M_Z$ distribution. Both published ALEPH event-shape analyses [12, 31] apply this correction. The ISR correction is not yet implemented in the current analysis and represents a systematic gap relative to the published results; its expected impact and planned implementation are discussed in Sec. 8.

The unfolding step consumes four synchronized inputs:

- detector-level data tree (`t`),

Sample	Total entries	Selected entries
1994 data reco	1,365,440	1,326,312
1994 MC reco	771,597	751,861
1994 MC gen (<code>tgen</code>)	771,597	771,597
1994 MC gen-before (<code>tgenBefore</code>)	973,769	973,769

Table 1. Nominal sample bookkeeping for the thrust unfolding chain. Selected entries correspond to `passEventSelection=1`. For generator-level trees, all entries are retained by construction.

- detector-level MC tree (`t`),
- generator-level MC tree used for response matching (`tgen`),
- generator-level MC tree before hadronic event selection (`tgenBefore`).

The ratio `tgenBefore/tgen` is used to derive the hadronic event-selection correction applied after unfolding. Event matching between reco and gen levels is performed with the unique event identifier. For response filling, generator entries are matched to the reconstructed selected-event identifier set, consistent with the matched-response construction described in Sec. 7.

In addition to the archived baseline MC, alternative modern generator predictions — PYTHIA 8.3, Herwig 7.3, and Sherpa 2.2 — are used in this note through event-level reweighting variations to estimate theory-model dependence. These variations are propagated as dedicated systematic components in the final uncertainty model while preserving the same detector-response baseline.

Table 1 summarizes the event counts in the nominal thrust workflow. The archived MC reco sample contains approximately 772k selected events compared to 1.33M in data, giving a data-to-MC ratio of roughly 1.8. This imbalance means that MC statistical fluctuations contribute at a non-negligible level to the response matrix and that response-bin precision is limited by MC statistics in thrust bins where both data and MC counts are low.

6 Event reconstruction and selection

This section describes particle selection, hadronic event definition, and particle-category data/MC validation before unfolding. This validation is essential because the selected particles are the direct inputs to the thrust algorithm.

6.1 Particle categories and `pwflag` mapping

ALEPH reconstructed particles are categorized with an integer label `pwflag`. Table 2 summarizes the categories used in this analysis.

The archived reconstruction stores these objects as energy-flow candidates built from combined tracking and calorimetric information. Charged categories are anchored by high-quality tracking measurements, while neutral categories are anchored by calorimeter response. This object representation is the direct input to thrust, so any category-dependent detector mismatch appears as a potential migration effect in the unfolding response.

<code>pwflag</code>	Category
0	charged tracks
1	charged leptons (tracker + ECAL category)
2	charged leptons (tracker + muon category)
3	V^0 candidates
4	photons
5	neutral hadrons

Table 2. Particle-category labels used in archived ALEPH reconstructed events.

Selection item	Requirement
Charged category	<code>pwflag</code> $\in [0, 2]$
Charged acceptance	$ \cos\theta \leq 0.94$
Charged transverse momentum	$p_T \geq 0.2$ GeV
Charged impact parameter	$ d_0 \leq 2$ cm
Charged longitudinal impact	$ z_0 \leq 10$ cm
Charged hit quality	$N_{\text{TPC}} \geq 4$
Neutral category	<code>pwflag</code> $\in [3, 5]$
Neutral energy	$E \geq 0.4$ GeV
Neutral acceptance	$ \cos\theta \leq 0.98$
Neutral hadron cleaning	reject <code>pwflag=5</code> for $-0.19 \leq \cos\theta < -0.18$
Use charged objects	<code>keepChargedTracks = True</code> (nominal)
Use neutral objects	<code>keepNeutralTracks = True</code> (nominal)

Table 3. Object-level selections used to build the nominal thrust input particle set, with one line per requirement.

All selected charged and neutral categories contribute to the thrust numerator and denominator through their momentum vectors. Therefore, mismodeling in any category can bias the detector-level event-shape response and the unfolded result.

6.2 Object-level and event-level selections

Table 3 lists the object-level nominal selection with one requirement per row. These criteria define which reconstructed particles are propagated into thrust and therefore which detector effects enter the response model.

The nominal hadronic event selection is summarized in Table 4, also with one line per requirement.

In practice, these selections enforce a phase space with high tracking quality, controlled forward acceptance, and stable visible-energy topology before entering event-shape reconstruction. They are chosen to follow ALEPH-standard hadronic selections while retaining explicit control over the regions that dominate event-shape sensitivity.

The neutral hadron cleaning requirement (reject `pwflag=5` for $-0.19 \leq \cos\theta < -0.18$) removes a localized region where the ALEPH hadronic calorimeter response is known to produce spurious neutral-hadron candidates. This narrow angular window corresponds to

Selection item	Requirement
Ntuple preselection	<code>passesNTupleAfterCut = 1</code>
Total charged energy	$E_{\text{trk}}^{\text{tot}} \geq 15 \text{ GeV}$
Sphericity-axis acceptance	$ \cos \theta_{\text{Sph}} \leq 0.82$
Charged multiplicity	$N_{\text{trk}} \geq 5$
Total multiplicity	$N_{\text{trk}} + N_{\text{neu}} \geq 13$
Visible energy guard	$E_{\text{vis}} \geq 0 \text{ GeV}$ (nominally inactive)
Missing-momentum guard	$ \vec{p}_{\text{miss}} < 9999 \text{ GeV}$ (nominally inactive)

Table 4. Nominal event-level hadronic selection requirements, including guards present in code but inactive in the nominal configuration.

a structural gap in the detector and was identified from the data/MC neutral-hadron $\cos \theta$ distribution.

V^0 candidates (`pwflag=3`) include K_S and Λ from displaced-vertex reconstruction. These objects enter the thrust sum with their measured momentum vector rather than individual decay products, which is consistent with treating them as single hadronic objects for event-shape purposes. Their contribution to the thrust numerator and denominator is captured by the neutral-response systematic variations.

6.3 Particle-category kinematic validation

Before constructing thrust-family observables, we validate the reconstructed particle-level ingredients that enter the event-shape sums and axis determination. Any mismodeling in particle acceptance, momentum scale, or category composition can propagate into migration in the detector response matrix and into unfolded distributions. To assess detector modeling of these inputs, we compare data and MC reco distributions for each `pwflag` category using Data/MC ratio panels, with generator-level references from `tgen` and `tgenBefore`. These validation plots are taken from the dedicated validation snapshot with the same nominal selection configuration used for the current thrust workflow.

Figures 1–6 provide the full variable-by-variable checks for each reconstructed particle category that contributes to thrust. In each case, the same observable set is shown to keep the detector-level validation uniform across categories: angular acceptance, momentum scale, and quality-related variables are all checked before constructing event-shape observables. In Fig. 1, the charged-track category drives the event-shape denominator and axis finding, so agreement here anchors the full detector response modeling. The $\cos \theta$ distribution shows the expected enhancement away from the acceptance edges and a falloff near the fiducial boundary, while the d_0 and z_0 spectra are concentrated in the high-quality track region selected for the nominal sample. The N_{TPC} , p_T , and energy panels provide direct checks that tracking-quality and hard-track tails are described with the precision required for stable thrust unfolding.

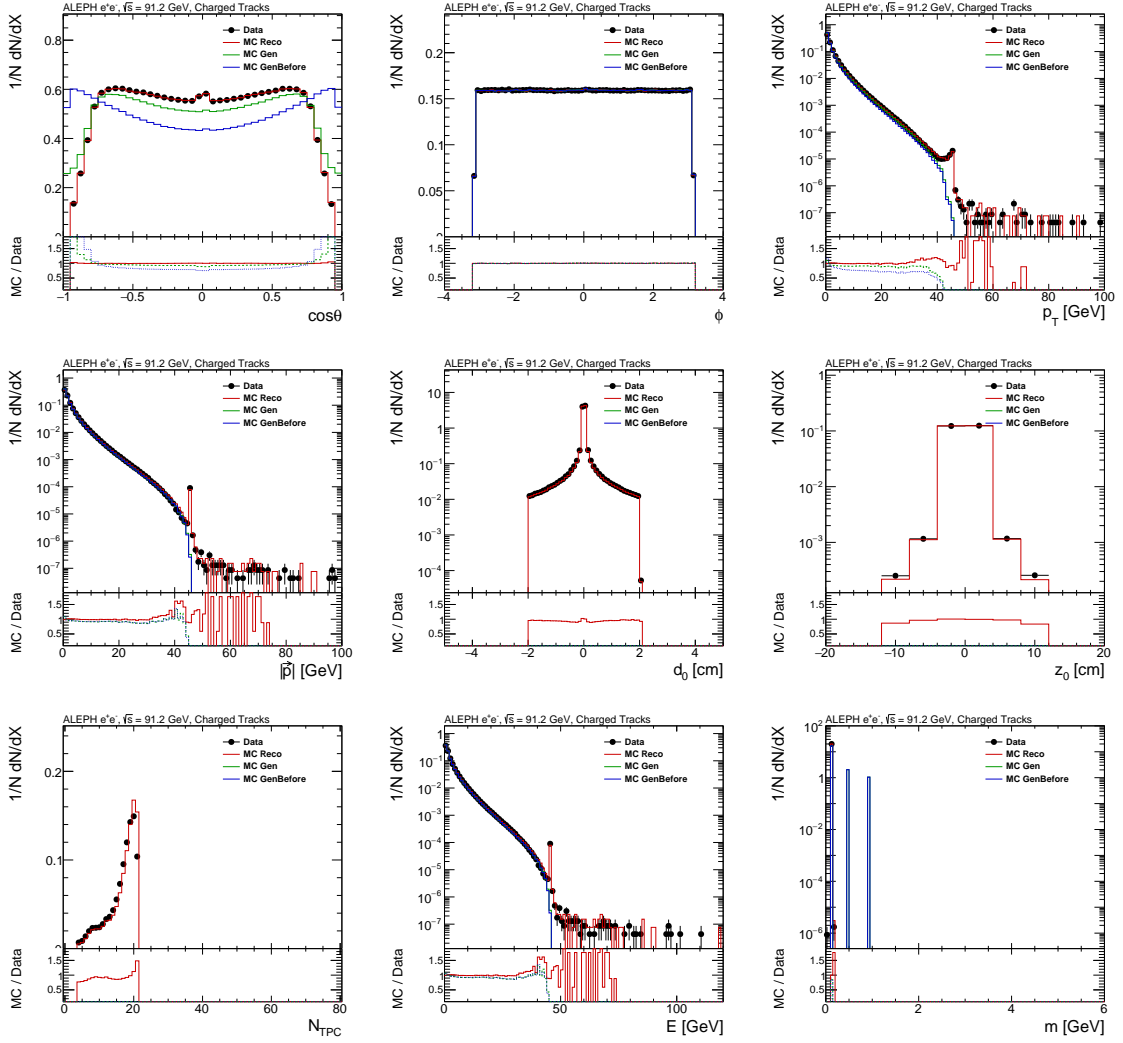


Figure 1. Complete $p_{wflag}=0$ kinematic set.

Figure 2 shows the first charged-lepton class used in the nominal object list; these lower-rate objects still affect event axes in asymmetric topologies. Relative to charged tracks, this category has smaller yields and larger statistical fluctuations, but the detector-level and MC shapes remain consistent across the main selection observables. The comparison is important because isolated energetic leptons can rotate the thrust axis in otherwise two-jet-like events and can therefore influence migration in specific bins.

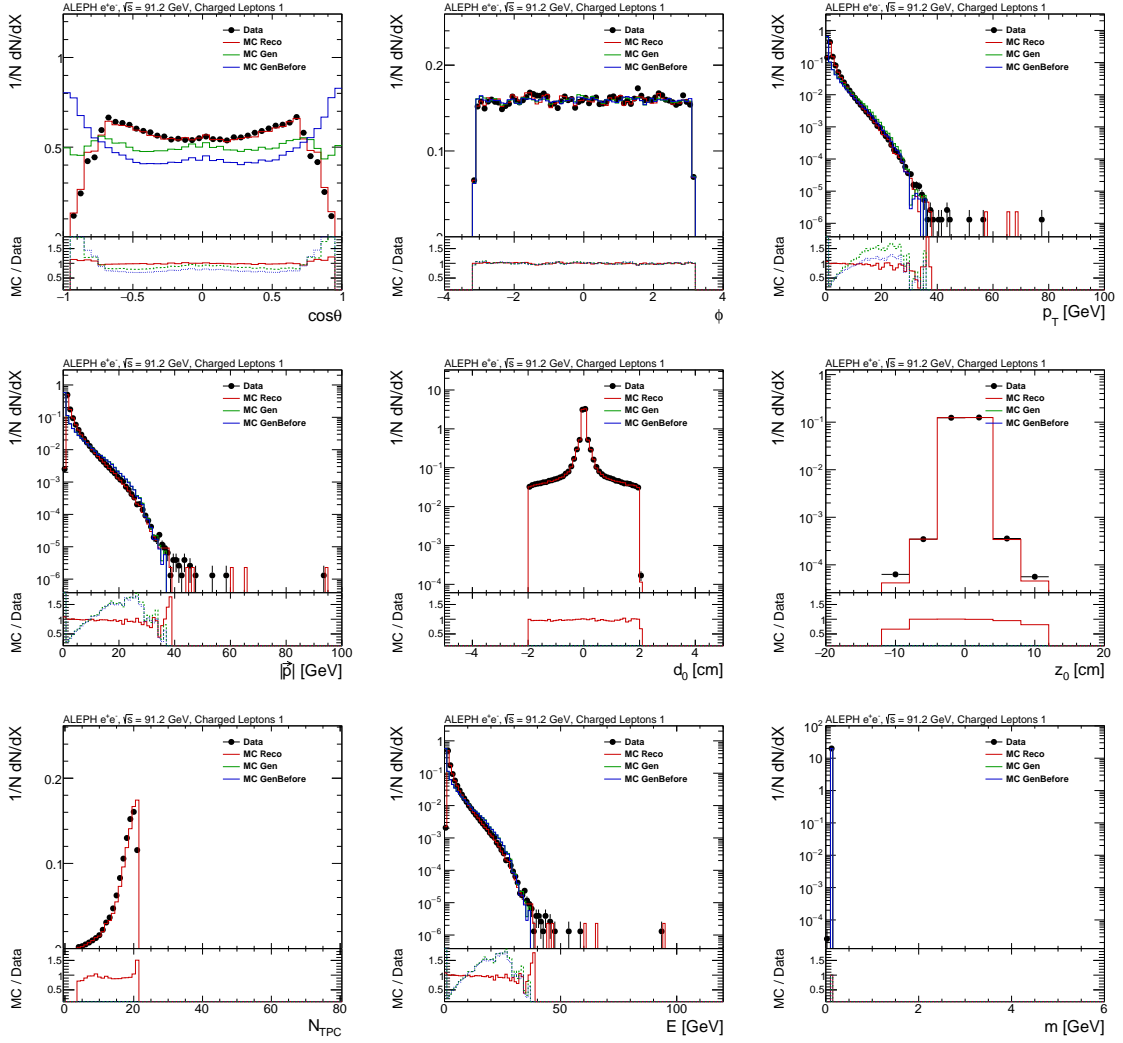


Figure 2. Complete $p_{wflag}=1$ kinematic set.

Figure 3 presents the second charged-lepton category, providing a direct cross-check of category-dependent acceptance and momentum-shape modeling. This category probes objects with different subdetector signatures than Fig. 2, so agreement here confirms that lepton-category partitioning does not induce a hidden detector asymmetry in the thrust inputs. The high- p_T and high-energy tails are monitored explicitly because even a small mismodeling there can project onto endpoint thrust bins.

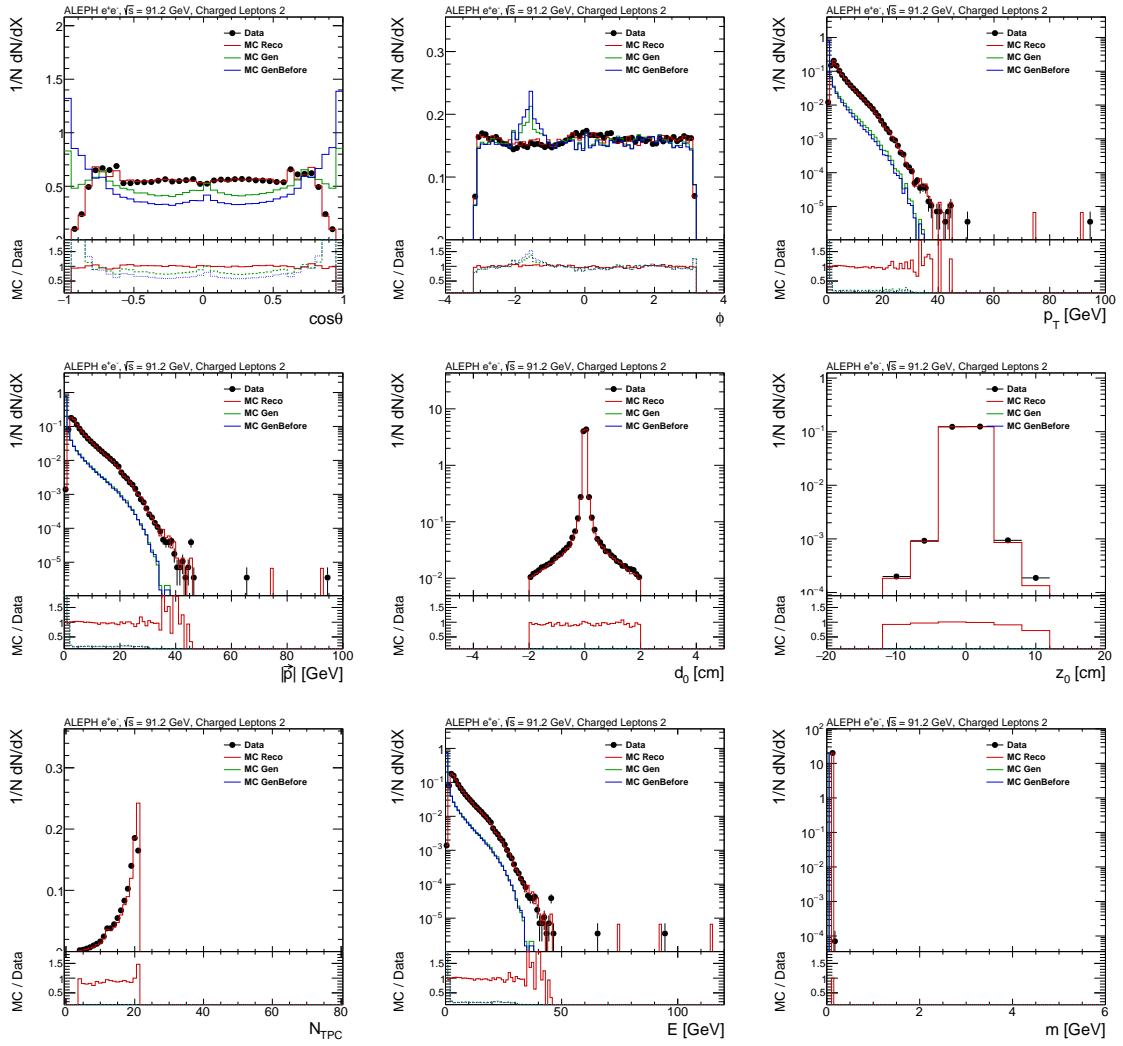


Figure 3. Complete $p_{wflag}=2$ kinematic set.

Figure 4 begins the neutral-object categories, where angular and energy modeling are especially relevant for visible-energy flow in thrust reconstruction. For this category, the energy spectrum and angular acceptance are the primary physics handles for event shape modeling, while the track-like quantities provide consistency checks of the archived object classification. Agreement in this panel supports a controlled transfer of neutral energy flow into the unfolded thrust response.

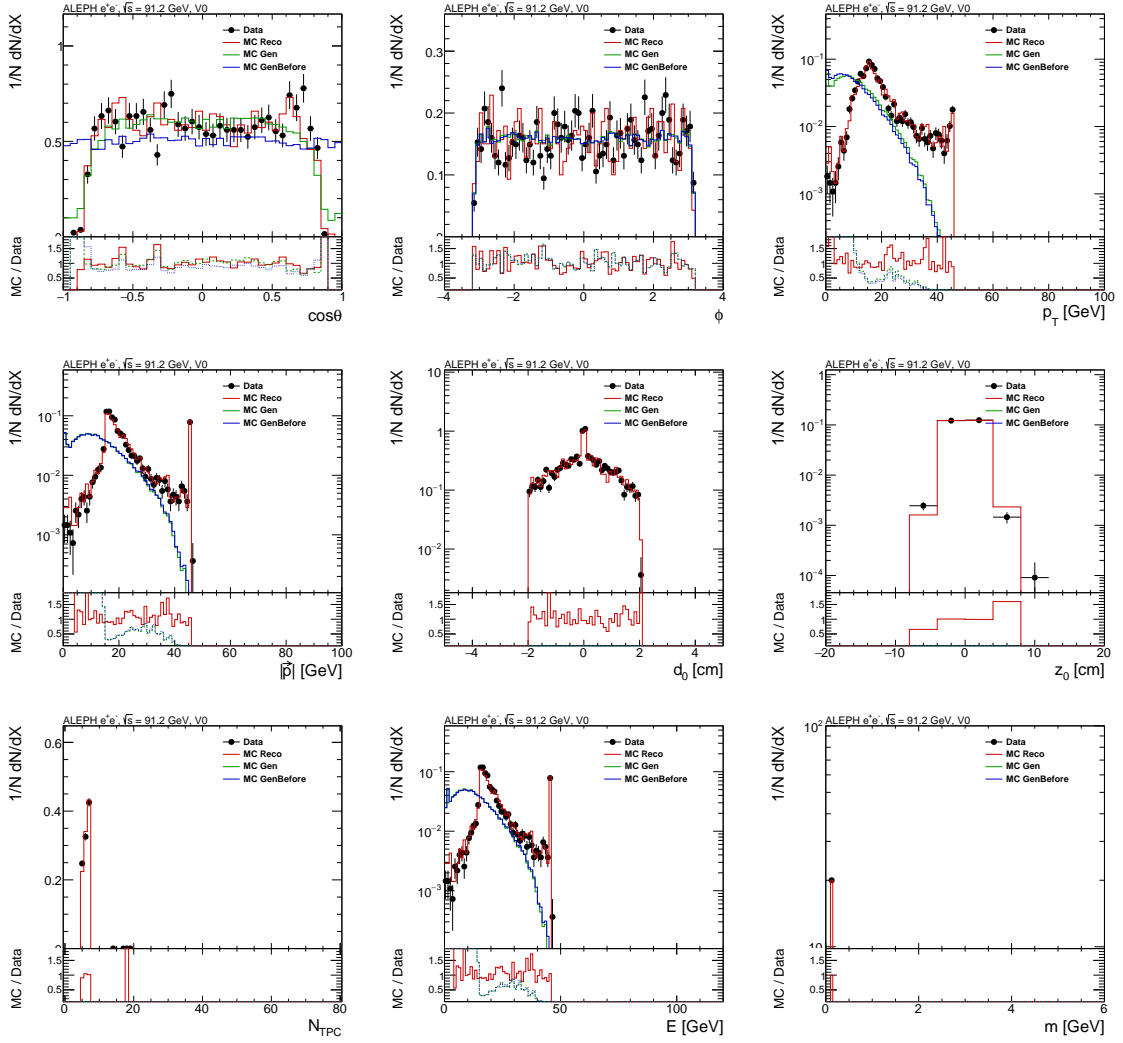


Figure 4. Complete $p_{wflag}=3$ kinematic set.

Figure 5 isolates photons, which probe neutral electromagnetic response and its effect on event-shape normalization. The photon energy and angular spectra are especially important because electromagnetic neutral energy contributes directly to visible event topology and hemisphere energy balance. The observed data/MC consistency in the core region supports the neutral-energy calibration assumptions used in the nominal unfolding and neutral-response systematic variations.

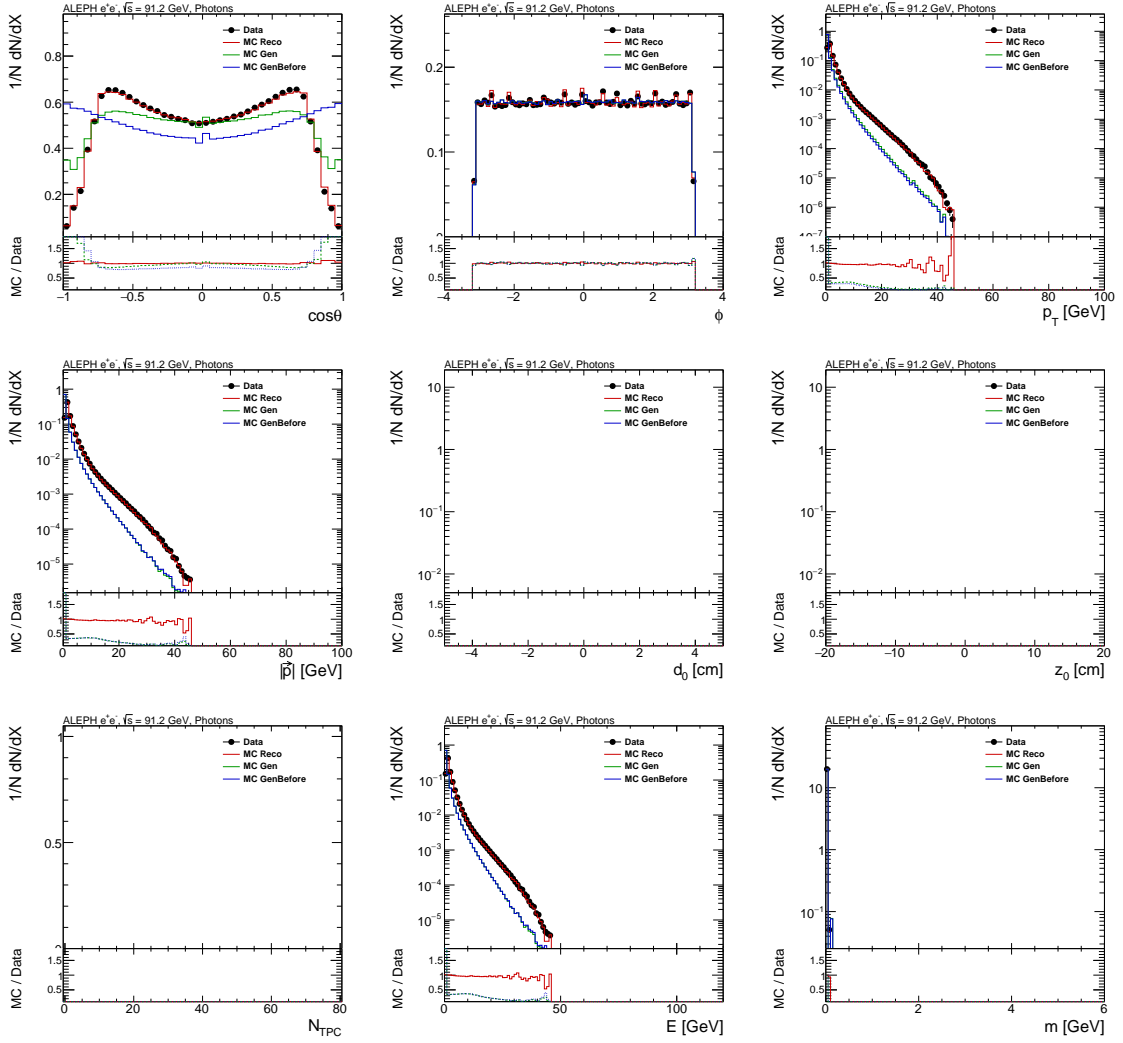


Figure 5. Complete $p_{wflag}=4$ kinematic set.

Figure 6 completes the neutral-hadron validation; this category is a key input for neutral-response systematics propagated to the unfolded thrust result. This category is typically softer and more sensitive to HCAL response and acceptance boundaries, so it is a direct stress test of the neutral part of the thrust model. The remaining differences in low-statistics tails are propagated through dedicated neutral-response and cross-check branches in the experimental systematic program, rather than absorbed into ad hoc selections.

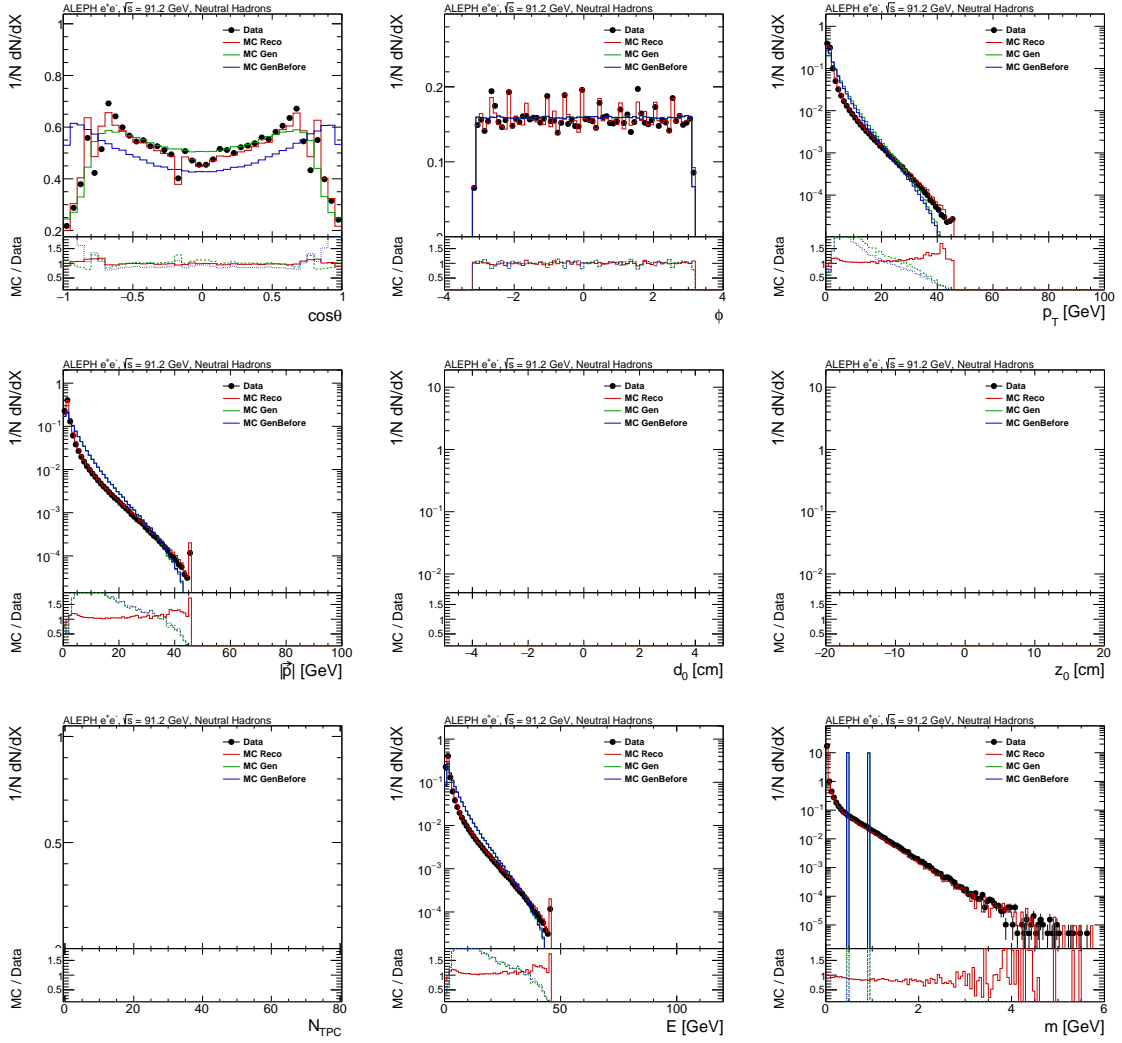


Figure 6. Complete `pwflag=5` kinematic set.

`pwflag=0` (charged tracks). Figure 1 is the dominant detector-modeling anchor for this analysis because charged tracks provide most of the selected-particle multiplicity and momentum flow. Data/MC agreement is good in the bulk of all distributions. The $\cos\theta$ panel shows the geometric acceptance cutoff at $|\cos\theta| = 0.94$, with consistent data/MC behavior across the accepted range. The impact-parameter panels (d_0 , z_0) show the effect of the nominal selection quality cuts, with both data and MC reproducing the expected Gaussian core and non-Gaussian tails. The N_{TPC} distribution shows good overall agreement between generators, with small differences between JETSET and modern generators in the tail region.

`pwflag=1` and `2` (ECAL-matched and muon-matched leptons). Figures 2 and 3 show the two charged-lepton categories. These are lower-rate than charged tracks. Data/MC agreement is satisfactory in the bulk of the kinematic distributions. Differences between the archived MC and modern generators (Pythia 8, Herwig, Sherpa) are visible in

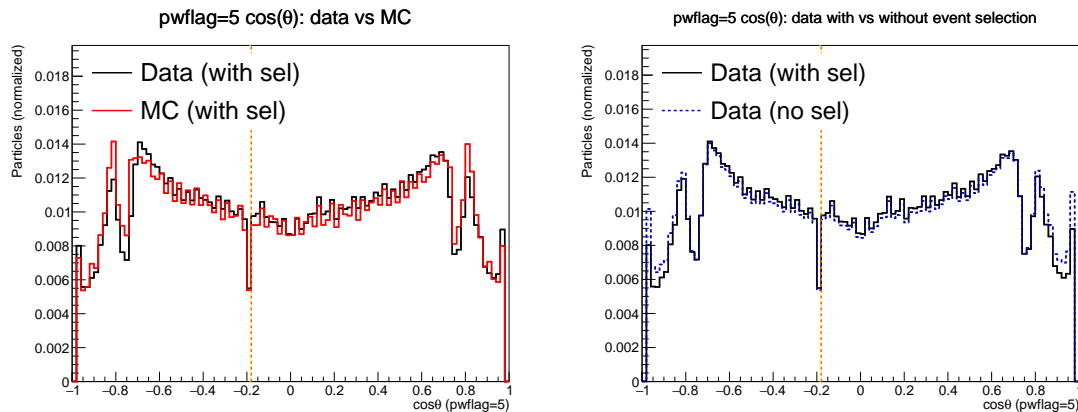


Figure 7. Left: $\cos\theta$ for $\text{pwflag}=5$ (neutral hadrons), data vs MC with event selection applied; the yellow band marks the cleaning cut region $-0.19 \leq \cos\theta < -0.18$. Right: data with vs without event selection, showing the suppression introduced by the cut.

the energy tails, which reflect generator-dependent differences in leptonic event rates and fake-lepton modeling.

pwflag=3 (V^0 candidates). Figure 4 shows K_S^0 and Λ candidates from displaced-vertex reconstruction. These enter the thrust sum as single four-vectors. Data/MC agreement in the bulk $\cos\theta$ and energy distributions is adequate. Generator differences are more visible than for charged tracks, reflecting differences in strange-particle production modeling.

pwflag=4 (photons). Figure 5 shows the photon category reconstructed by the ECAL. Data/MC agreement is good in the central angular region. The ϕ spectrum (Fig. 5) shows a modulation in the generator-level distribution; this feature and its origin are under investigation (see Sec. 6.3).

pwflag=5 (neutral hadrons). Figure 6 shows the neutral hadronic calorimeter objects. The $\cos\theta$ distribution shows a visible suppression in the narrow window $-0.19 \leq \cos\theta < -0.18$, which is the result of the neutral hadron cleaning cut applied at that angular position. Figure 7 compares the $\cos\theta$ distribution with and without the cleaning cut, isolating the raw detector feature from the selection effect.

Generator differences between the archived ALEPH MC and modern generators are largest in this category, reflecting known differences in neutral hadronic energy modeling in the 1–2 GeV range. These differences are propagated through the dedicated neutral-response systematic branches and do not affect the nominal response matrix.

The ϕ spectrum excess visible in generator-level particles for photons and neutral hadrons (Fig. 5 and Fig. 6) may reflect JETSET 7.4 generator effects or the periodic modular structure of the ALEPH HCAL (24 iron absorber modules in ϕ). Figure 8 shows the ϕ distribution for $\text{pwflag}=4$ (photons) and $\text{pwflag}=5$ (neutral hadrons), comparing data, MC reco, and MC gen. Vertical lines mark the 24 HCAL module boundaries. The modulation is present in both reco and gen MC distributions but not at the same phase in data, suggesting the excess is primarily of generator (JETSET 7.4) origin rather than a

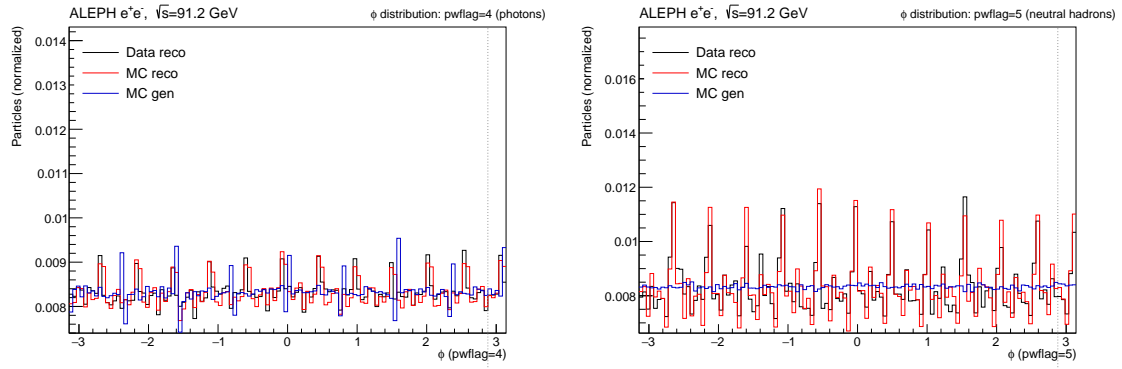


Figure 8. ϕ distribution for pwflag=4 photons (left) and pwflag=5 neutral hadrons (right), comparing data reco, MC reco, and MC gen. Dashed vertical lines mark the 24-fold HCAL module boundaries. The modulation present in MC reco and gen but absent in data at the same phase points to a generator-level origin.

detector ϕ -acceptance effect. It is retained as a cross-check and noted as a known difference between the archived MC and modern generators.

The modulation is present in both reconstructed and generator-level MC distributions but is absent from data at the same phase, pointing to a generator (JETSET 7.4) origin rather than a detector acceptance effect. Because it cancels between MC reco and gen in the response matrix, it does not bias the unfolded thrust distribution; it is retained here as a cross-check and documented difference between the archived MC and modern generators.

6.4 Event-level selection observables

Event-level variables used for hadronic selection are also validated with data/MC comparisons, as shown in Fig. 9. These observables summarize the selected particle content and accepted topology that define the phase space used to build detector response and unfolded event-shape spectra.

The event-level panels close the logic between object-level selections and the final sample entering event-shape reconstruction. N_{trk} and $N_{\text{trk}} + N_{\text{neu}}$ test whether multiplicity thresholds sculpt data and MC in a consistent way; this is critical because those same multiplicities enter hadronic-event preselection and determine which events contribute to response filling. E_{Ch} checks charged-energy modeling near the hadronic-selection boundary at 15 GeV, and $\cos\theta_{\text{Sph}}$ tests whether accepted event topology is similarly contained in detector acceptance for data and MC.

Overall agreement in the high-statistics regions supports the response-model baseline used for IBU. The visible differences are concentrated in lower-populated tails and near selection boundaries, where statistical fluctuations and detector-response limitations are expected to be larger. These regions are not ignored: their impact is propagated through the experimental systematic program and is reflected in the final uncertainty decomposition.

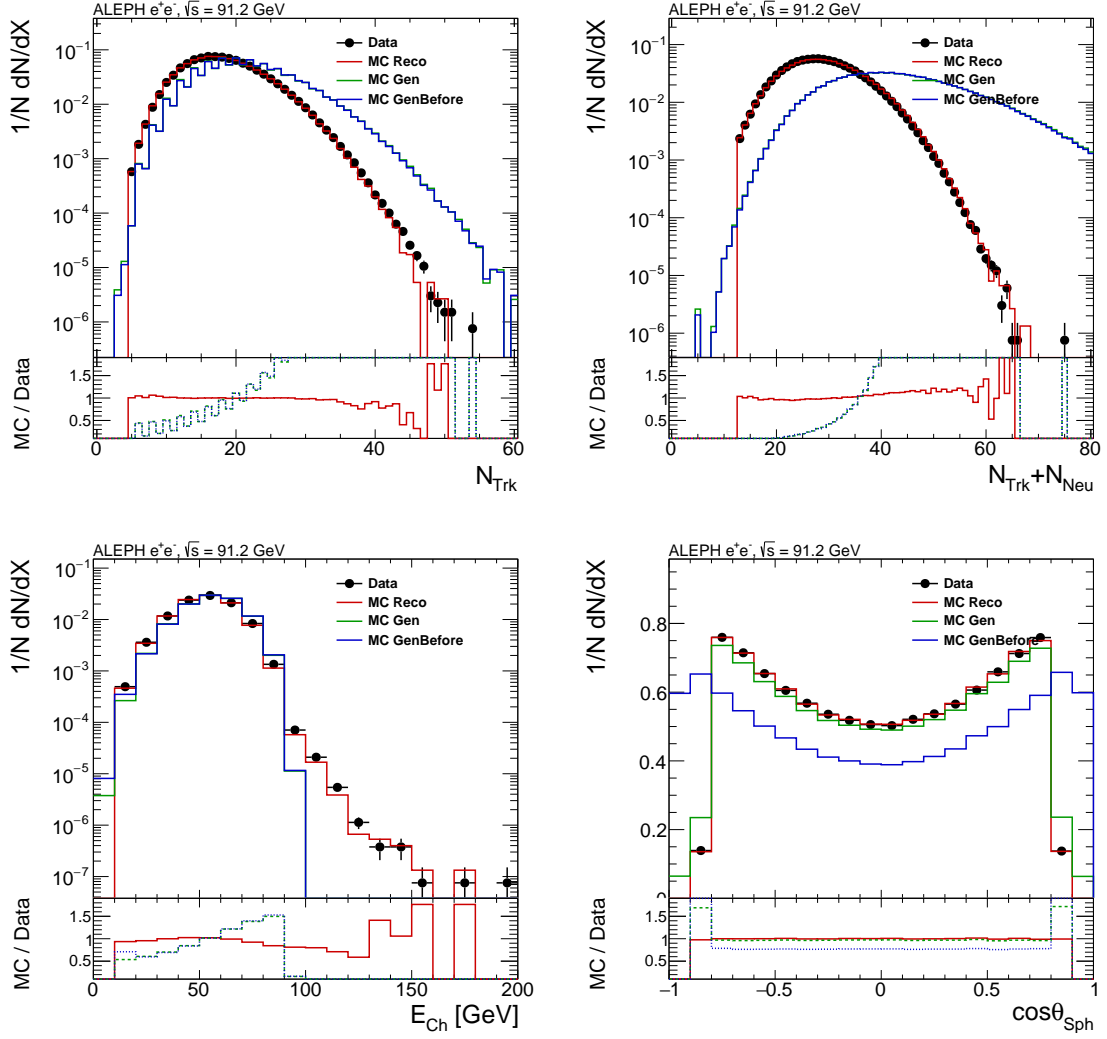


Figure 9. Event-level observables used in the nominal hadronic selection; legends include detector-level data/MC and generator-level references.

Item	Nominal configuration
Observable	Thrust T
Range	$0.5 \leq T < 1.0$
Binning	50 uniform bins
Reco/gen matching key	<code>uniqueID</code>
Reco selection branch	<code>passEventSelection</code>
Nominal IBU iterations	5
Hadronic correction	enabled ($N_{\text{genBefore}}/N_{\text{gen}}$)
Statistical covariance input	unfolding covariance transformed to normalized differential-thrust basis
RooUnfold covariance method	<code>kCovariance</code> (analytical error propagation)
Particle-level target	stable hadrons ($c\tau > 10$ mm), inclusive over full hadronic Z phase space

Table 5. Nominal analysis configuration used in the thrust Iterative Bayesian Unfolding workflow.

7 Analysis method

This section documents the thrust analysis method, including the observable definition, the response construction, the unfolding setup, systematic execution, and the correction and covariance workflow. Executable workflow details, command sequences, and pseudocode are collected in Appendix A to keep the main text focused on physics.

7.1 Observable definition and nominal configuration

The thrust observable is defined as [18]

$$T = \max_{\hat{n}} \frac{\sum_i |\vec{p}_i \cdot \hat{n}|}{\sum_i |\vec{p}_i|}, \quad (7.1)$$

with all selected charged and neutral reconstructed objects from Sec. 6 entering the sum. We first adopt bins identical to the published ALEPH event-shape analysis [12], using 50 uniform bins over $0.5 \leq T < 1.0$ (bin width $\Delta T = 0.01$), which enables a direct bin-by-bin comparison with the published ALEPH result. We then test fine bins throughout the full thrust space to assess the usable binning resolution in different regions, particularly in the high-thrust (low $\tau = 1 - T$) regime. The thrust resolution study in Sec. 7.4 informs the finest binning achievable in each region.

The nominal run uses $N_{\text{iter}} = 5$ and applies the post-unfolding hadronic event correction from `tgenBefore/tgen`. The nominal branch is the only run with covariance enabled; variation branches are propagated through signed shifts relative to the nominal spectrum.

7.2 Response construction from matched MC

Response filling uses event-by-event matching through `uniqueID`. Reconstructed MC entries with `passEventSelection` equal to 1 define the selected detector-level phase space. Generator-level entries are then matched to this selected set and used to fill:

- the response counts matrix;
- the miss term required by RooUnfold for inefficiency handling.

This matched-response construction enforces a consistent phase-space definition between detector-level selection and generator-level truth used in unfolding. Generator-level events with no matched reco entry (misses, from reconstruction inefficiency or acceptance gaps) are handled by RooUnfold’s efficiency correction. Reco-level events with no matched gen entry (fakes, from beam background or random coincidences) are not expected to be significant in the archived ALEPH hadronic sample and are not separately subtracted.

7.3 Iterative Bayesian Unfolding setup and iteration choice

Detector correction is performed with RooUnfold Bayesian unfolding,

$$U_j^{(n+1)} = \frac{1}{\epsilon_j} \sum_i M_i \frac{R_{ij} \pi_j^{(n)}}{\sum_k R_{ik} \pi_k^{(n)}}, \quad (7.2)$$

where M_i is the measured detector-level spectrum, R_{ij} is the response, and $\pi_j^{(n)}$ is the iteration prior.

The prior for the first iteration is taken as the generator-level MC truth distribution $\pi_j^{(0)} = N_{\text{gen}}(j)$, the standard RooUnfold default. This choice initializes the unfolding close to the expected truth shape and avoids any flat-prior amplification of high-frequency fluctuations in the first iteration.

The nominal regularization is

$$N_{\text{iter}} = 5, \quad (7.3)$$

with $N_{\text{iter}} = 4$ and 6 propagated as unfolding-regularization systematic branches. The iteration-choice diagnostics, including refolded spectra at $N = 4, 5, 6, 10, 100$ compared with detector-level data, confirm that the closure-shape χ^2/ndf is stable and that the iteration-to-iteration change in the unfolded spectrum is small for $N_{\text{iter}} \in \{4, 5, 6\}$.

The response matrix has a diagonal fraction of $f_{\text{diag}} = 0.33$, meaning approximately two-thirds of events migrate out of their generated thrust bin at reconstruction level. This level of bin-to-bin migration is expected for thrust at ALEPH given the finite charged-particle momentum resolution and the sensitivity of thrust to soft particles near the event boundary. It implies that the unfolding correction is non-trivial and that the choice of regularization strength meaningfully affects the result. This provides confidence that $N_{\text{iter}} = 5$ sits in a well-regularized plateau rather than near an instability. The propagated $N_{\text{iter}} = 4, 6$ systematic covers residual regularization-bias uncertainty at the level documented in Sec. 8.

The “miss” term—generator-level events with no matched reconstructed counterpart—is documented in Fig. 10. These are events that fail the reco-level hadronic event selection despite being generated within the fiducial volume. The miss rate is concentrated at low thrust ($T \lesssim 0.7$) and in events with low charged multiplicity, consistent with the hadronic event selection removing poorly reconstructed events. RooUnfold accounts for miss events via `response.Miss(x_{gen})`, which correct the unfolded spectrum for this acceptance effect.

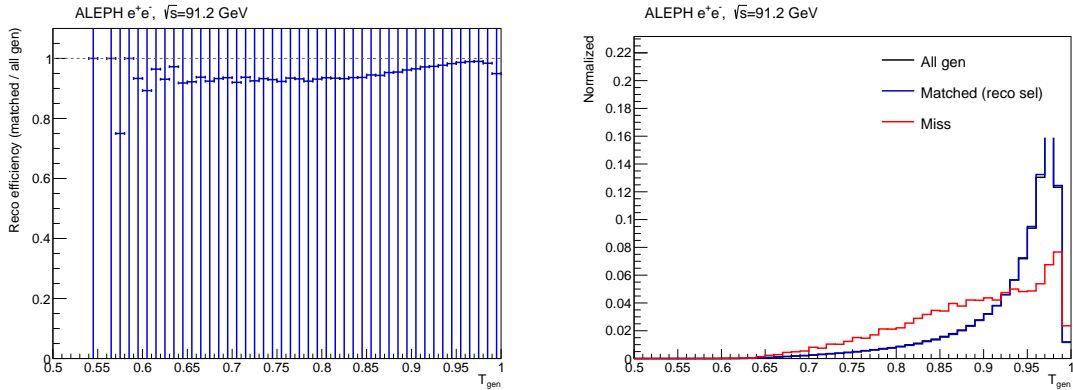


Figure 10. Left: reco efficiency (matched/all gen) as a function of T_{gen} . Right: thrust distributions for all gen, matched, and miss events (normalized to unit area). Miss events are concentrated at low thrust and low multiplicity, consistent with events failing the hadronic event selection.

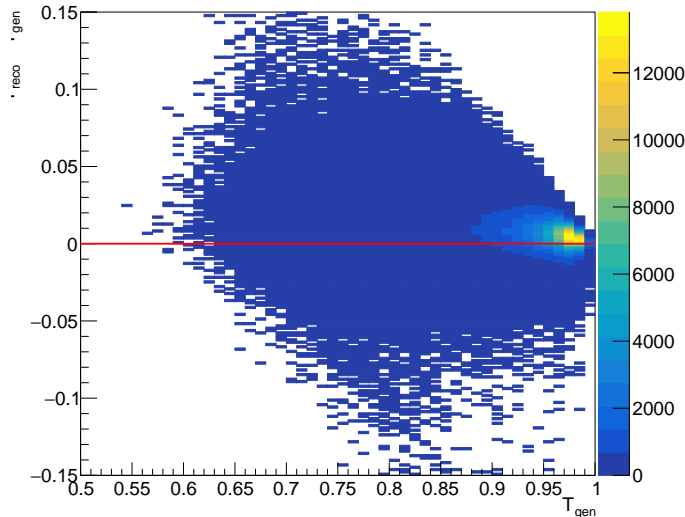


Figure 11. Distribution of $(T_{\text{reco}} - T_{\text{gen}})$ for matched MC event pairs, integrated over all T_{gen} . The distribution is narrow and centered at zero, confirming no significant systematic bias in the thrust reconstruction.

7.4 Thrust resolution study

The usable binning resolution is characterized using matched reco–gen event pairs. Figure 11 shows the distribution of $(T_{\text{reco}} - T_{\text{gen}})$ integrated over all thrust values. The distribution is narrow and centered at zero, confirming no significant systematic bias. The resolution narrows toward $T \rightarrow 1$, motivating finer binning in the high-thrust region. The previous ALEPH analyses [12] chose bin sizes “somewhat smaller than twice the corresponding detector resolution,” and our IBU approach uses this principle to guide the finest bins.

Component	Inputs	Combination rule
Iteration	<code>iter4, iter6</code>	Envelope per bin: $\max \Delta_{\text{iter}} $
Track/event	<code>ntpc7, pt04, ech10, with_met</code>	Quadrature of absolute shifts
Neutral	<code>nes_up, nes_down, ner</code>	NES envelope, then quadrature with NER
Theory	<code>pythia8, herwig, sherpa</code>	Envelope across generators
Hadronic corr.	<code>tgen/tgenBefore</code> ratio	Propagated bin-by-bin
Exp. total	track/event + neutral	$\Delta_{\text{exp}} = \sqrt{\Delta_{\text{t/e}}^2 + \Delta_{\text{neu}}^2}$
Total	stat + iter + exp + theory + had	$\Delta_{\text{tot}} = \sqrt{\Delta_{\text{stat}}^2 + \Delta_{\text{iter}}^2 + \Delta_{\text{exp}}^2 + \Delta_{\text{th}}^2 + \Delta_{\text{had}}^2}$
<i>Cross-check</i>	<i><code>no_neutrals</code></i>	<i>Diagnostic only; excluded from total</i>

Table 6. Systematics combination scheme for the thrust baseline. Each row gives the input systematic variations and the combination rule used to form the per-bin uncertainty contribution. The experimental subtotal (Exp. total) and final total are formed by quadrature of their respective sub-components. The cross-check branch (`no_neutrals`) is used for stress-testing only.

7.5 Systematics execution map

Systematic branches are executed by rerunning unfolding with variation-specific inputs or theory weights, then converting each branch into a signed shift relative to nominal. The combination structure is summarized in Table 6.

The nominal total uncertainty model (Sec. 8) combines component magnitudes in quadrature after branch-specific envelope or quadrature rules. The `no_neutrals` branch is retained as a stress-test and explicitly reported, but excluded from the nominal total.

7.6 Hadronic correction, ISR correction, covariance propagation, and matrix exports

After unfolding, a bin-wise hadronic event-selection correction is applied,

$$C_{\text{had}}(j) = \frac{N_{\text{genBefore}}(j)}{N_{\text{gen}}(j)}, \quad U_j^{\text{corr}} = U_j C_{\text{had}}(j). \quad (7.4)$$

Following the hadronic correction, an ISR correction is applied bin-by-bin to remove the contribution of initial-state photon radiation that shifts the centre-of-mass energy below the Z -pole:

$$C_{\text{ISR}}(j) = \frac{N_{\text{noISR}}^{\text{gen}}(j)}{N_{\text{ISR}}^{\text{gen}}(j)}, \quad U_j^{\text{final}} = U_j^{\text{corr}} C_{\text{ISR}}(j). \quad (7.5)$$

The numerator and denominator are taken from standalone PYTHIA8 samples generated with ISR disabled (`isr0_ALL.root`) and enabled (`isr1_ALL.root`), respectively, using the `tgenBefore/thrust` branch (stored as $1-T$, transformed back to T). The ratio histograms are pre-computed once into a cache file and applied identically to the nominal and all systematic variation branches, so that the ISR correction cancels in the systematic shifts and its residual uncertainty (from finite MC statistics on the ratio) is propagated as a separate component Δ_{ISR} (Sec. 8.5).

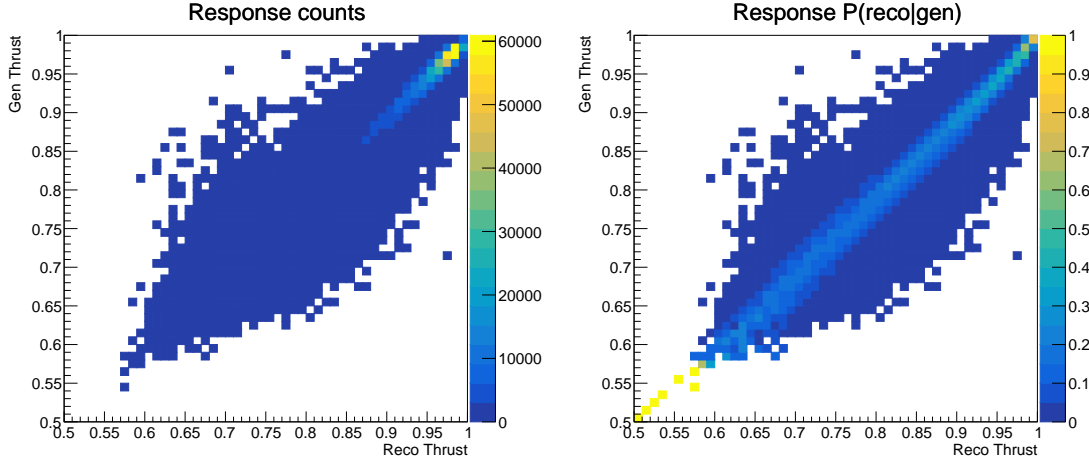


Figure 12. Nominal response matrices for thrust: response counts (left) and response probability (right).

For the nominal run, the statistical covariance is computed by RooUnfold using analytical error propagation (`RooUnfold::kCovariance`), which propagates Poisson uncertainties in the data and response histograms through the IBU iteration chain without toy MC sampling. The resulting covariance matrix is read from the unfolding output and transformed to the normalized differential-thrust basis used in this note. Non-statistical component covariances are built with a configurable model (nominal: `template_correlated`), and fit-window covariance products are exported together with full-range matrices by `build_prelim_uncertainty_summary.py`.

Response and matrix visualizations are exported by the matrix-plot helper script (see Appendix A for details). Full provenance metadata for the run, including git commit, ROOT version, RooUnfold version, environment fingerprint, response diagnostics, theory-weight coverage, and all computed uncertainty metrics, is written to a structured JSON summary file. This file is the primary machine-readable record of the result and is the canonical reference for any numeric claims in Sec. 9.

The nominal and systematics execution logic, including command sequences, pseudocode for workflow control and uncertainty assembly, and the reproduction contract for this note, are documented in Appendix A.

8 Systematic uncertainties

Systematic variations are propagated by rerunning the full unfolding chain for each variation and comparing to the nominal unfolded result. For each source v , the signed bin-wise shift is

$$\delta_v(j) = \frac{U_v(j) - U_{\text{nom}}(j)}{U_{\text{nom}}(j)}. \quad (8.1)$$

The sources are grouped into six independent components: statistical, unfolding-regularization, experimental detector, theory modeling, hadronic event-selection correction, and ISR cor-

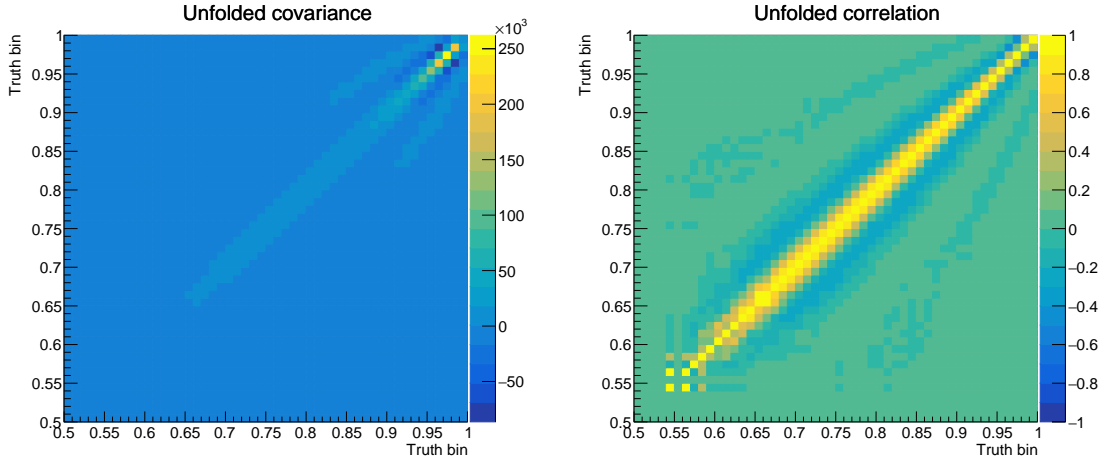


Figure 13. Nominal unfolded covariance matrix (left) and corresponding correlation matrix (right).

rection. The sections below describe each component and its physics motivation before presenting the combination model and numerical results.

8.1 Statistical uncertainty

The statistical uncertainty arises from Poisson fluctuations in the $\sim 700,000$ hadronic-event data sample. It is propagated analytically by RooUnfold (`RooUnfold::kCovariance`) through the IBU iteration chain, without toy-MC sampling, yielding a full statistical covariance matrix $\text{Cov}_{ij}^{(\text{stat})}$. The per-bin fractional uncertainty $\Delta_{\text{stat}}(j) = \sqrt{\text{Cov}_{jj}^{(\text{stat})}}/U_j^{\text{corr}}$ is small and nearly uniform across the spectrum, typically below 2% in the central range, owing to the high statistics of the 1994 ALEPH dataset.

The unfolding regularization uncertainty is closely related: two additional unfolding passes at $N_{\text{iter}} = 4$ and $N_{\text{iter}} = 6$ quantify the sensitivity of the result to the regularization choice. The iteration envelope $\Delta_{\text{iter}}(j) = \max(|\delta_{\text{iter}4}(j)|, |\delta_{\text{iter}6}(j)|)$ is sub-percent in the bulk of the spectrum, confirming that the nominal $N_{\text{iter}} = 5$ sits on a stable plateau and that regularization is not a limiting source of uncertainty. Figure 14 shows the signed per-bin shifts for both components across the measurement range.

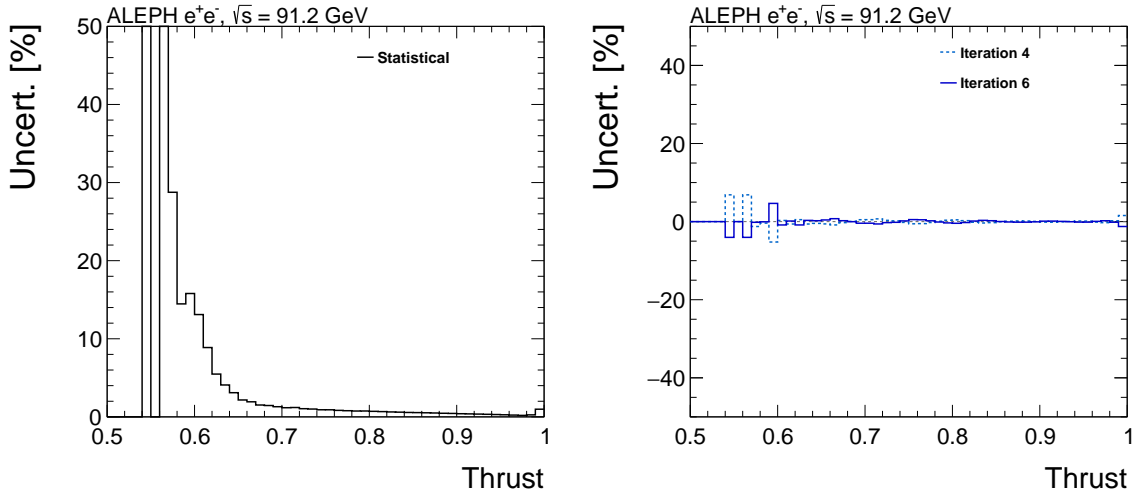


Figure 14. Signed per-bin shifts for the statistical (left) and unfolding-iteration (right) uncertainty components. The statistical component is nearly flat and small across the spectrum. The iteration panel shows $N_{\text{iter}} = 4$ and 6 relative to the nominal $N_{\text{iter}} = 5$; the envelope (dashed black) is sub-percent in the bulk, confirming a stable regularization plateau.

Group	Branch	What is varied	Combination
Track/event	<code>ntpc7</code>	TPC hit requirement $N_{\text{TPC}} > 7$ (nominal > 4)	Quadrature of four shifts
	<code>pt04</code>	Charged $p_T > 0.4$ GeV threshold (nominal > 0.2 GeV)	
	<code>ech10</code>	Charged-energy cut > 10 GeV (nominal > 15 GeV)	
	<code>with_met</code>	Missing- E_T added as pseudo-particle	
Neutral response	<code>nes_up/dn</code>	Neutral energies scaled up/down; probes ECAL energy-scale	Envelope then quadrature with ner
	<code>ner</code>	Neutral objects randomly removed; probes reco efficiency	Quadrature with nes envelope

Table 7. Experimental systematic variations. Track/event branches are combined in quadrature; neutral-response branches as envelope+quadrature. Δ_{exp} is the quadrature sum of the two sub-totals.

8.2 Experimental systematic uncertainties

Experimental systematic variations probe detector response effects that could bias the reconstructed thrust distribution. Seven branches are defined, divided into two sub-groups: track/event selection and neutral-object response, summarized in Table 7.

The four track/event variations are combined in quadrature:

$$\Delta_{\text{track/event}}(j) = \sqrt{\sum_{v \in \{\text{ntpc7}, \text{pt04}, \text{ech10}, \text{with_met}\}} |\delta_v(j)|^2}. \quad (8.2)$$

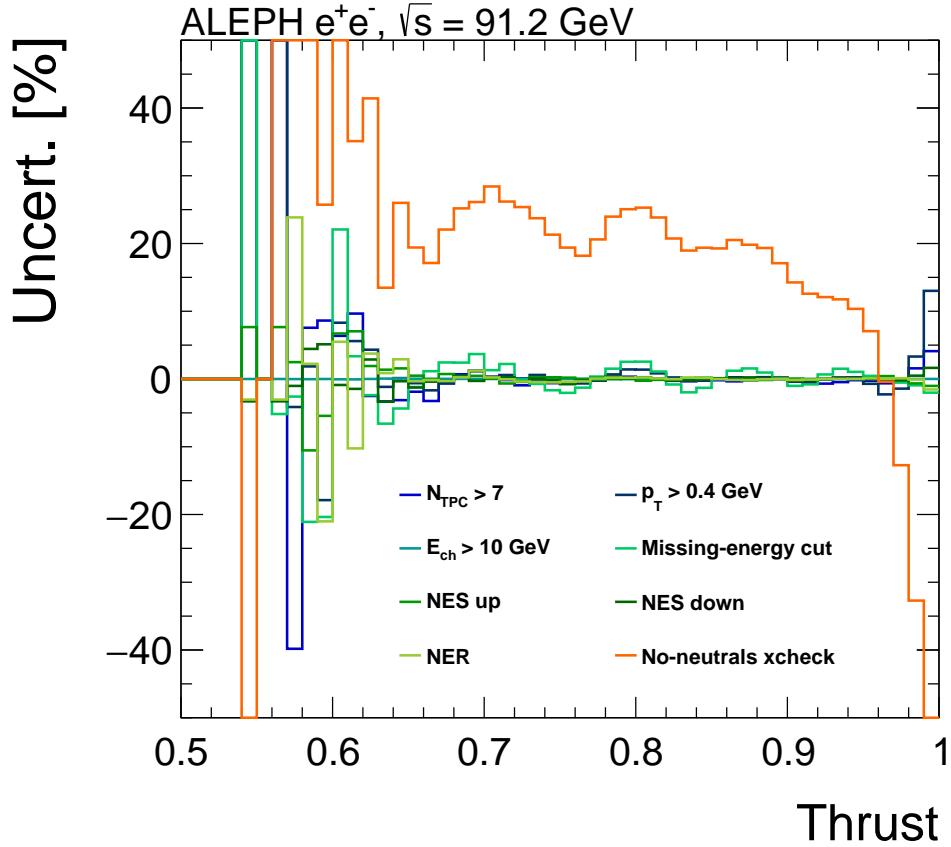


Figure 15. Signed per-bin shifts for the seven experimental variation branches, with the group envelope (dashed black). The four track/event branches (`ntpc7`, `pt04`, `ech10`, `with_met`) and three neutral-response branches (`nes_up`, `nes_down`, `ner`) are shown; the y -axis is clipped to $\pm 50\%$.

The three neutral-object response variations are combined as:

$$\Delta_{\text{neutral}}(j) = \sqrt{\max(|\delta_{\text{nes_up}}(j)|, |\delta_{\text{nes_down}}(j)|)^2 + |\delta_{\text{ner}}(j)|^2}. \quad (8.3)$$

The full experimental envelope is then

$$\Delta_{\text{exp}}(j) = \sqrt{\Delta_{\text{track/event}}^2(j) + \Delta_{\text{neutral}}^2(j)}. \quad (8.4)$$

Figure 15 shows the signed per-bin shifts for all seven branches. The largest contributions arise at low thrust ($T \lesssim 0.62$) where the steeply rising spectrum amplifies small absolute shifts; in the central range the experimental envelope is typically 5–15%.

The neutral-object response variations are chosen in preference to a simpler approach of removing all neutral particles from the event. The fundamental reason is that removing neutrals entirely redefines the observable: the resulting distribution is no longer the energy-flow thrust T_{EF} but a different quantity, charged-only thrust T_{ch} , computed from a different particle-level definition. Treating the difference $T_{\text{EF}} - T_{\text{ch}}$ as a systematic uncertainty on

the energy-flow measurement would conflate two distinct observables and produce an uncertainty that is unphysically large. Instead, `nes_up`, `nes_down`, and `ner` vary the detector response to neutral objects while holding the particle-level definition fixed, providing a physically meaningful probe of calorimeter modeling uncertainties without changing what is being measured.

To quantify this distinction, the full unfolding chain was repeated with neutral particles (`pwflag` \in $\{4, 5\}$) removed, yielding a charged-only thrust distribution. Both the energy-flow and charged-only results are processed through the complete analysis chain — IBU with $N_{\text{iter}} = 5$, hadronic correction $C_{\text{had}}(j)$, and ISR correction $C_{\text{ISR}}(j)$ — using separate response matrices for each particle-level definition. Both distributions are shown with statistical uncertainties only; the full systematic suite is not propagated for this diagnostic comparison, and the charged-only branch is excluded from the nominal total uncertainty combination.

The charged-only spectrum is systematically softer than the energy-flow result at low thrust, as expected from the missing neutral-energy deposits. In the central range the mean shift is approximately 23% — a magnitude that could not plausibly represent a detector uncertainty on the energy-flow measurement, confirming that the two distributions correspond to fundamentally different observables. No pathological bin-level disagreement is observed, confirming that the neutral-hadron cleaning cut (Sec. 6.2) does not introduce a bias in the energy-flow thrust distribution. Figure 16 shows the comparison.

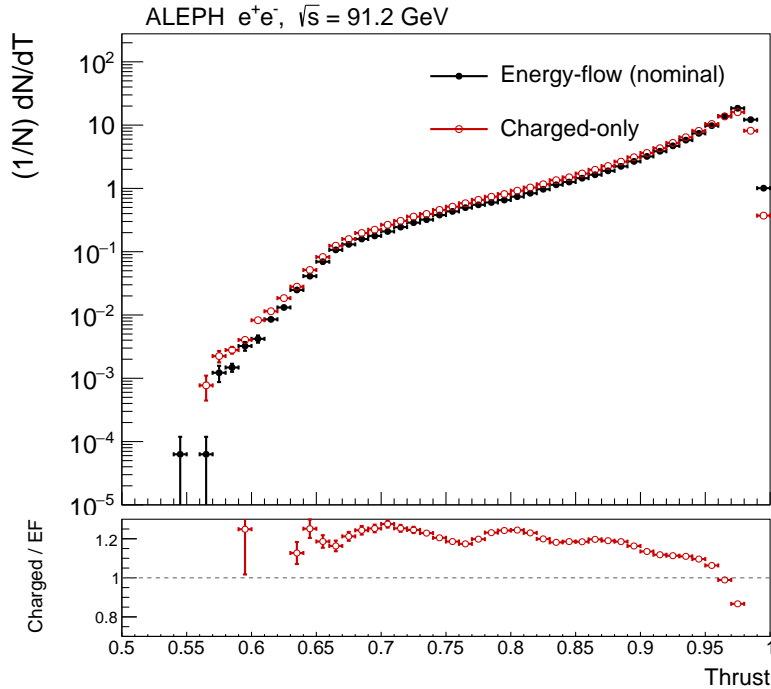


Figure 16. Comparison of the charged-only (red open circles) and energy-flow (black filled circles) unfolded thrust distributions. Both are processed through the complete analysis chain: IBU ($N_{\text{iter}} = 5$), hadronic correction $C_{\text{had}}(j)$, and ISR correction $C_{\text{ISR}}(j)$, with separate response matrices for each particle-level definition. Error bars represent statistical uncertainties only. Both distributions are normalized to $(1/N) dN/dT$. The ratio panel shows charged-only / energy-flow; the dashed line marks unity. The $\sim 23\%$ central-range shift reflects the different particle-level definitions of the two observables, not a detector systematic effect, motivating the use of neutral-response variations (`nes_up`, `nes_down`, `ner`) to probe calorimeter uncertainties within the energy-flow observable.

8.3 Theory systematic uncertainties

Theory systematic variations probe the residual model dependence introduced by the Monte Carlo generator used to build the detector response matrix. The nominal response matrix is constructed from Jetset 7.4/Pythia 6, the ALEPH simulation. Three additional generators are used to reweight the generator-level thrust distribution event-by-event, producing alternative response matrices that span a wide range of parton-shower algorithms and hadronization models: `pythia8` (Pythia 8 with Monash tune, dipole-ordered shower), `herwig` (Herwig 7.3, angular-ordered shower with cluster hadronization), and `sherpa` (Sherpa with AHADIC++ hadronization). The theory envelope is taken as the maximum absolute shift across the three generators:

$$\Delta_{\text{theory}}(j) = \max(|\delta_{\text{pythia8}}(j)|, |\delta_{\text{herwig}}(j)|, |\delta_{\text{sherpa}}(j)|). \quad (8.5)$$

All three generators agree well with the nominal at high thrust ($T > 0.95$) but diverge progressively at lower thrust where soft-gluon emission and hadronization effects are largest.

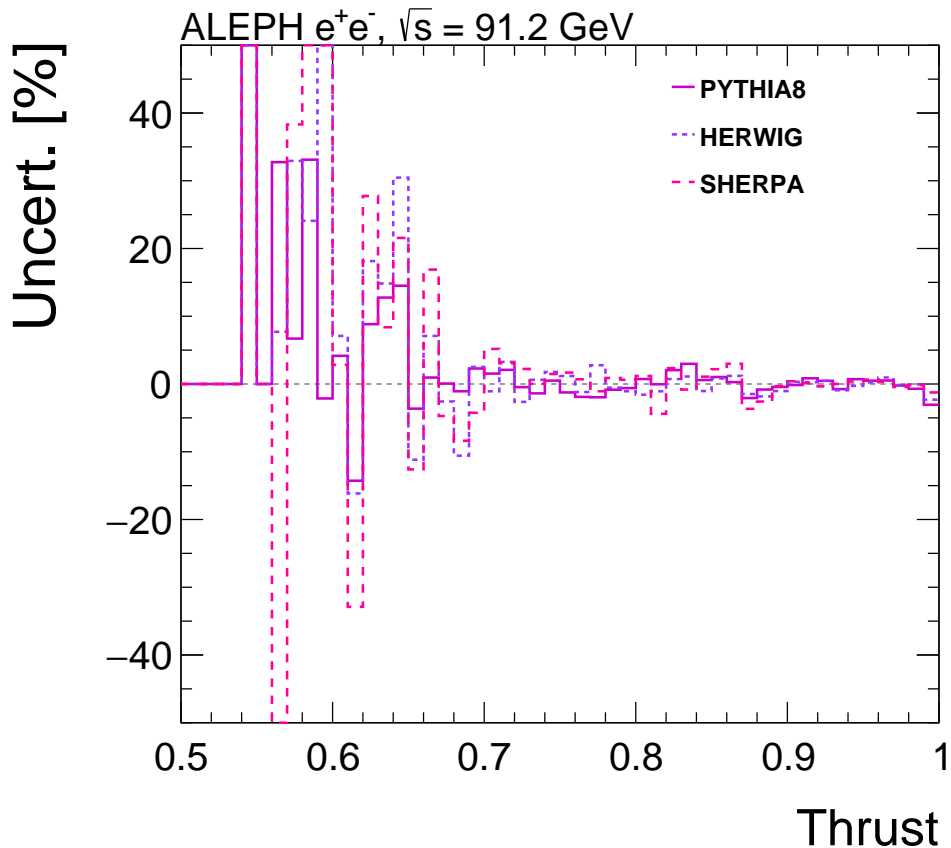


Figure 17. Signed per-bin shifts for the three theory reweighting branches (`pythia8`, `herwig`, `sherpa`) with the theory envelope (dashed black). Generator differences grow at lower thrust, reflecting parton-shower and hadronization modeling uncertainties. This is the dominant source across the central measurement range. The y -axis is clipped to $\pm 50\%$.

The theory envelope is the dominant uncertainty contribution across the central measurement range, as shown in Figure 17.

8.4 Hadronic event-selection correction

After unfolding, a bin-wise hadronic event-selection correction is applied to account for the fraction of hadronic events lost to the generator-level selection:

$$C_{\text{had}}(j) = \frac{N_{\text{genBefore}}(j)}{N_{\text{gen}}(j)}, \quad U_j^{\text{corr}} = U_j C_{\text{had}}(j). \quad (8.6)$$

This correction maps the unfolded spectrum from the generator-level hadronic-event-selected phase space to the full stable-hadron level, as described in Sec. 5. The uncertainty on this correction is propagated as an independent component Δ_{had} .

The correction ratio $C_{\text{had}}(j)$ is computed from two generator-level histograms: `tgenBefore` (events before hadronic selection) and `tgen` (events passing hadronic selection). Statisti-

cal uncertainties on both histograms are propagated through the ratio using standard error propagation, yielding bin-wise up and down variations $C_{\text{had}}^{\pm}(j)$. These variations are applied to the unfolded spectrum and normalized to the differential cross-section basis, producing up and down shifted spectra. The fractional hadronic correction uncertainty is then defined as the envelope:

$$\delta_{\text{had}}^{\pm}(j) = \frac{U_j \cdot C_{\text{had}}^{\pm}(j) / \int U \cdot C_{\text{had}}^{\pm} dT}{U_j^{\text{corr}}} - 1, \quad (8.7)$$

with $\Delta_{\text{had}}(j) = \max(|\delta_{\text{had}}^{+}(j)|, |\delta_{\text{had}}^{-}(j)|)$.

8.5 ISR correction

An initial-state radiation (ISR) correction removes the contribution of events where the e^+e^- center-of-mass energy is reduced by photon radiation before the hard scatter, mapping the measured distribution from the ISR-inclusive sample to the pure $\sqrt{s} = M_Z$ distribution:

$$C_{\text{ISR}}(j) = \frac{N_{\text{noISR}}^{\text{gen}}(j)}{N_{\text{ISR}}^{\text{gen}}(j)}. \quad (8.8)$$

Both published ALEPH event-shape analyses apply this correction [12, 31]. The 1998 ALEPH analysis [31] defines it as the ratio of generator-level thrust distributions produced with and without ISR, using JETSET 7.4. The 2004 analysis [12] uses KORALZ, which provides a more accurate treatment of ISR, to generate the corrected distribution.

The ISR correction is applied bin-by-bin after the hadronic correction using standalone PYTHIA8 samples with ISR disabled (`isr0`) and enabled (`isr1`), as described in Sec. 7.6. The uncertainty on this correction is derived from the finite Monte Carlo statistics of the ratio $C_{\text{ISR}}(j) = N_{\text{noISR}}^{\text{gen}}(j)/N_{\text{ISR}}^{\text{gen}}(j)$ using standard error propagation:

$$\sigma_{\text{rel}}(j) = \sqrt{\left(\frac{\sigma_{N_0}(j)}{N_0(j)}\right)^2 + \left(\frac{\sigma_{N_1}(j)}{N_1(j)}\right)^2}, \quad (8.9)$$

where N_0 and N_1 are the ISR-OFF and ISR-ON histogram contents with their Poisson errors. Up and down variations $C_{\text{ISR}}^{\pm}(j) = C_{\text{ISR}}(j) \cdot (1 \pm \sigma_{\text{rel}}(j))$ are applied to the unfolded spectrum and the envelope is taken as $\Delta_{\text{ISR}}(j)$. The uncertainty is purely MC-statistical in nature; the PYTHIA8 generator used here differs from the KORALZ generator used in the ALEPH 2004 analysis [12], which provides a more accurate ISR description. This difference in generator is not propagated as an additional systematic in the current release.

8.6 Statistical covariance

For the nominal run, the statistical covariance is computed by RooUnfold using analytical error propagation (`RooUnfold::kCovariance`), which propagates Poisson uncertainties in the data and response histograms through the IBU iteration chain without toy MC sampling. The resulting covariance matrix is read from the unfolding output and transformed to the normalized differential-thrust basis used in this note.

Non-statistical component covariances are built with a configurable model. The current nominal release uses the `template_correlated` option, where each non-statistical component covariance is built as

$$\text{Cov}_{ij}^{(c)} = \Delta_c(i) \Delta_c(j) \rho_{ij}^{\text{stat}}, \quad (8.10)$$

with ρ_{ij}^{stat} taken from the statistical unfolding covariance correlation template. This keeps component magnitudes tied to the measured per-bin shifts while avoiding a purely diagonal systematic-covariance approximation. For cross-check studies, `diagonal` and `block` component models are also available.

8.7 Combination model

The total bin uncertainty combines all six components in quadrature:

$$\Delta_{\text{tot}}(j) = \sqrt{\Delta_{\text{stat}}^2(j) + \Delta_{\text{iter}}^2(j) + \Delta_{\text{exp}}^2(j) + \Delta_{\text{theory}}^2(j) + \Delta_{\text{had}}^2(j) + \Delta_{\text{ISR}}^2(j)}. \quad (8.11)$$

The `no_neutrals` branch (charged-only thrust) is explicitly excluded from this combination. It is not a physical variation of the energy-flow measurement but a stress-test of the analysis sensitivity to neutral-object contributions; its role as a diagnostic cross-check is discussed in Sec. 8.2.

8.8 Uncertainty breakdown

Figure 18 shows the absolute fractional magnitudes of all uncertainty components as a compact 2×2 overview. Theory is the dominant source across the central range; the experimental envelope is typically 5–15% and largest at $T \lesssim 0.62$ where the steeply rising spectrum amplifies small absolute shifts. The statistical and iteration components remain sub-percent in the bulk, confirming that neither data statistics nor the regularization choice limits the measurement precision.

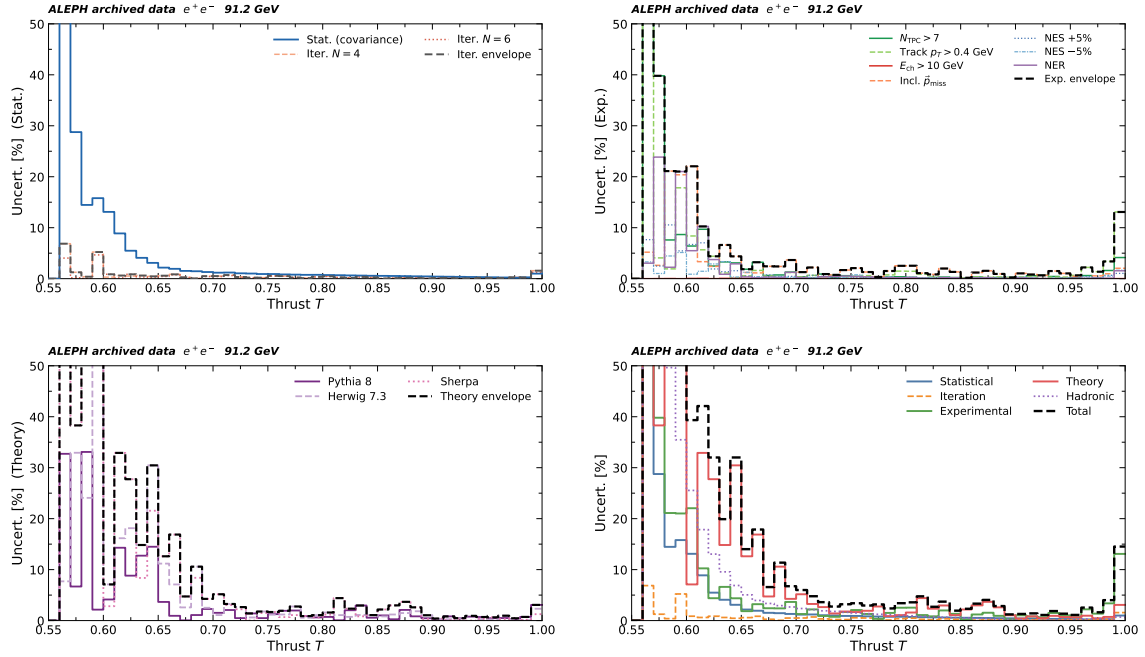


Figure 18. Absolute per-bin fractional uncertainties (y -axes limited to 50%). Top left: statistical and unfolding-iteration components. Top right: seven experimental variation branches with group envelope. Bottom left: theory reweighting branches with theory envelope. Bottom right: all groups overlaid; dashed black shows total.

9 Results

The thrust baseline result is obtained from the 1994 workflow with Iterative Bayesian Unfolding at nominal $N_{\text{iter}} = 5$, including the hadronic event correction, ISR correction, and all configured systematic reruns. All 14 nominal and systematic unfolding jobs completed successfully. The response matrix diagonal fraction is 0.332, indicating substantial migration between reconstructed and generated thrust bins.

9.1 Final unfolded thrust distribution

Figure 19 (left) shows the unfolded spectrum with the total uncertainty band and comparison to the published ALEPH 2004 result. Agreement is good across the bulk of the spectrum ($0.62 \leq T < 0.99$), with the largest discrepancy at the endpoint ($0.99 < T < 1.00$, ratio 1.30 ± 0.27). This is physically expected: the dijet limit is sensitive to MC modeling of soft hadrons, and the hadronic correction $C_{\text{had}}(j)$ and ISR correction $C_{\text{ISR}}(j)$ carry growing uncertainties there. Normalization convention differences between the current analysis and the 2004 ALEPH publication also contribute at the endpoint.

Figure 19 (right) shows direct comparison with OmniFold and prior IBU spectra from the archived-data analysis program. Sub-unity χ^2/ndf values reflect the conservative uncertainty model and positive off-diagonal correlations, not overestimation. Differences are localized to the endpoint region.

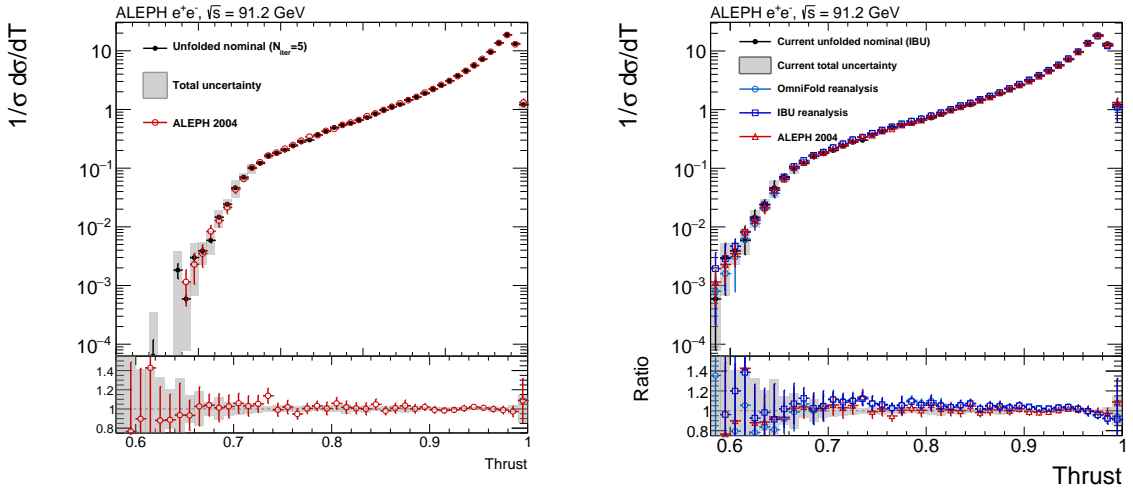


Figure 19. Left: final unfolded thrust distribution with total uncertainty band compared to the published ALEPH 2004 result. The ratio panel shows bin-by-bin agreement across the full measurement range, with the gray band representing the total uncertainty envelope. Right: comparison with OmniFold and prior IBU spectra; the ratio panel shows each method relative to the current unfolded nominal. Compatibility metrics are $\chi^2/\text{ndf} = 0.663$ (OmniFold), 0.421 (prior IBU), and 0.361 (ALEPH 2004), evaluated over 42 bins using the diagonal of the total covariance.

The total correlation matrix for the combined result is shown in Fig. 20. The off-diagonal structure is non-trivial: strong positive correlations appear in the high-thrust region where the theory and hadronic-correction components dominate and their shifts are coherent across bins. The maximum off-diagonal correlation is $|\rho_{ij}| = 0.889$, confirming that the full covariance matrix — rather than diagonal uncertainties alone — must be used in any downstream fit or comparison.

The numerical per-bin uncertainty breakdown is given in Tables 8–10, listing all component contributions and the total for each thrust bin.

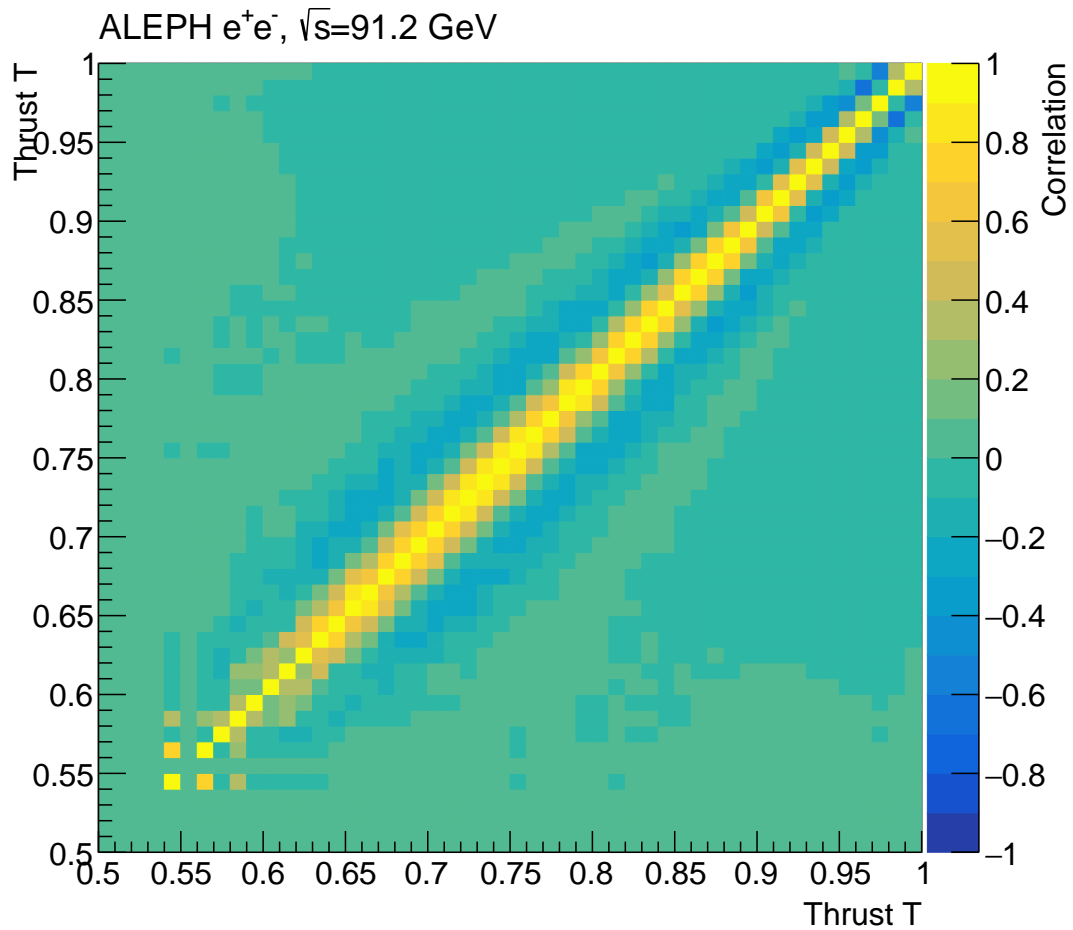


Figure 20. Total bin-to-bin correlation matrix for the final result, combining statistical, unfolding-iteration, experimental, theory, hadronic-correction, and ISR-correction components using the `template_correlated` covariance model. The maximum off-diagonal correlation is $|\rho_{ij}| = 0.889$.

T range	$(1/\sigma) d\sigma/dT$	Stat. [%]	Iter. [%]	Exp. [%]	Theory [%]	Had. corr. [%]	Total [%]
[0.55,0.56)				—			
[0.56,0.57)	6.30×10^{-5}	88.8	6.9	467.8	67.7	139.7	500.9
[0.57,0.58)	0.0012	28.8	1.2	46.7	38.3	70.5	97.2
[0.58,0.59)	0.0015	14.5	0.4	25.0	59.5	49.6	82.7
[0.59,0.60)	0.0032	15.8	5.2	35.8	53.5	35.5	75.3
[0.60,0.61)	0.0042	13.1	0.9	25.9	7.1	25.5	39.3
[0.61,0.62)	0.0085	8.9	0.6	17.1	32.9	17.8	42.1
[0.62,0.63)	0.0131	5.5	0.9	7.3	27.7	13.0	32.0
[0.63,0.64)	0.0248	4.1	0.6	8.2	14.8	9.6	19.9
[0.64,0.65)	0.0411	3.1	0.5	6.3	30.5	6.9	32.0
[0.65,0.66)	0.0695	2.2	0.6	2.6	12.6	5.0	14.0
[0.66,0.67)	0.1068	1.9	0.8	3.8	16.9	3.9	17.9
[0.67,0.68)	0.1305	1.5	0.3	2.7	4.7	3.4	6.6
[0.68,0.69)	0.1587	1.5	0.1	2.6	10.6	2.9	11.4
[0.69,0.70)	0.1776	1.3	0.5	4.3	4.3	2.7	6.7
[0.70,0.71)	0.2087	1.2	0.5	1.4	5.2	2.4	6.0
[0.71,0.72)	0.2448	1.2	0.7	2.4	3.3	2.1	4.8
[0.72,0.73)	0.2876	1.0	0.3	1.1	2.6	1.9	3.6
[0.73,0.74)	0.3210	1.0	0.2	1.2	1.4	1.8	2.8
[0.74,0.75)	0.3792	0.9	0.2	1.9	1.8	1.6	3.2
[0.75,0.76)	0.4332	0.9	0.6	2.3	1.7	1.5	3.4
[0.76,0.77)	0.4958	0.8	0.5	1.5	1.9	1.4	3.0
[0.77,0.78)	0.5504	0.8	0.2	0.5	2.8	1.2	3.2
[0.78,0.79)	0.5994	0.7	0.1	1.8	0.9	1.1	2.4
[0.79,0.80)	0.6550	0.8	0.4	3.0	1.1	1.0	3.4
[0.80,0.81)	0.7399	0.7	0.5	3.0	1.6	0.9	3.6
[0.81,0.82)	0.8395	0.7	0.3	1.4	4.4	0.8	4.8
[0.82,0.83)	0.9697	0.6	0.2	0.9	2.3	0.8	2.7
[0.83,0.84)	1.14	0.6	0.3	2.0	3.0	0.7	3.7
[0.84,0.85)	1.26	0.6	0.3	1.4	1.1	0.6	1.9
[0.85,0.86)	1.45	0.5	0.0	0.3	2.2	0.5	2.3
[0.86,0.87)	1.64	0.5	0.1	1.3	3.0	0.4	3.3
[0.87,0.88)	1.89	0.5	0.2	1.6	3.7	0.4	4.1
[0.88,0.89)	2.23	0.5	0.2	1.0	2.6	0.3	2.9
[0.89,0.90)	2.67	0.4	0.1	0.4	1.0	0.2	1.2
[0.90,0.91)	3.20	0.4	0.1	1.2	0.4	0.1	1.3
[0.91,0.92)	3.86	0.4	0.2	1.1	0.8	0.1	1.4
[0.92,0.93)	4.70	0.4	0.1	0.9	0.5	0.0	1.1
[0.93,0.94)	5.79	0.3	0.1	1.6	0.9	0.1	1.9
[0.94,0.95)	7.40	0.3	0.2	1.1	0.7	0.1	1.4
[0.95,0.96)	9.79	0.3	0.1	0.8	0.6	0.2	1.1
[0.96,0.97)	13.86	0.2	0.1	2.3	1.0	0.3	2.5
[0.97,0.98)	18.46	0.2	0.3	1.5	0.5	0.4	1.6
[0.98,0.99)	12.18	0.3	0.2	3.9	0.7	0.3	4.0
[0.99,1.00)	1.01	1.0	1.6	14.1	3.1	0.7	14.5

Table 8. Per-bin fractional uncertainties across the full measurement range ($0.55 \leq T < 1.0$). The second column gives the nominal unfolded $(1/\sigma) d\sigma/dT$ value; all remaining columns are absolute fractional uncertainties in percent. Bins with zero nominal spectrum (dashes) are below threshold. *Exp.* denotes the total experimental component (track/event and neutral sub-components combined in quadrature), and *Had. corr.* denotes the hadronic event-selection correction uncertainty.

T range	Our $(1/\sigma) d\sigma/dT$	Our total unc. [%]	ALEPH 2004 $(1/\sigma) d\sigma/dT$	ALEPH 2004 total unc. [%]
[0.55,0.56)	—	—	—	—
[0.56,0.57)	6.30×10^{-5}	500.9	—	—
[0.57,0.58)	0.0012	97.2	—	—
[0.58,0.59)	0.0015	82.7	0.0011	61.2
[0.59,0.60)	0.0032	75.3	0.0023	54.1
[0.60,0.61)	0.0042	39.3	0.0035	41.7
[0.61,0.62)	0.0085	42.1	0.0084	25.0
[0.62,0.63)	0.0131	32.0	0.0128	23.1
[0.63,0.64)	0.0248	19.9	0.0215	21.9
[0.64,0.65)	0.0411	32.0	0.0433	14.4
[0.65,0.66)	0.0695	14.0	0.0656	9.2
[0.66,0.67)	0.1068	17.9	0.1028	8.5
[0.67,0.68)	0.1305	6.6	0.1258	8.7
[0.68,0.69)	0.1587	11.4	0.1640	8.7
[0.69,0.70)	0.1776	6.7	0.1842	9.5
[0.70,0.71)	0.2087	6.0	0.2142	7.6
[0.71,0.72)	0.2448	4.8	0.2481	9.1
[0.72,0.73)	0.2876	3.6	0.2943	7.5
[0.73,0.74)	0.3210	2.8	0.3435	6.2
[0.74,0.75)	0.3792	3.2	0.3654	6.0
[0.75,0.76)	0.4332	3.4	0.4309	6.0
[0.76,0.77)	0.4958	3.0	0.4692	4.9
[0.77,0.78)	0.5504	3.2	0.5458	4.2
[0.78,0.79)	0.5994	2.4	0.5994	4.2
[0.79,0.80)	0.6550	3.4	0.6609	5.6
[0.80,0.81)	0.7399	3.6	0.7680	4.6
[0.81,0.82)	0.8395	4.8	0.8570	4.3
[0.82,0.83)	0.9697	2.7	0.9808	5.1
[0.83,0.84)	1.14	3.7	1.11	5.0
[0.84,0.85)	1.26	1.9	1.27	4.9
[0.85,0.86)	1.45	2.3	1.44	3.8
[0.86,0.87)	1.64	3.3	1.64	4.0
[0.87,0.88)	1.89	4.1	1.93	3.9
[0.88,0.89)	2.23	2.9	2.23	3.4
[0.89,0.90)	2.67	1.2	2.63	3.2
[0.90,0.91)	3.20	1.3	3.06	3.3
[0.91,0.92)	3.86	1.4	3.70	2.2
[0.92,0.93)	4.70	1.1	4.55	2.3
[0.93,0.94)	5.79	1.9	5.64	2.2
[0.94,0.95)	7.40	1.4	7.28	1.7
[0.95,0.96)	9.79	1.1	9.63	1.7
[0.96,0.97)	13.86	2.5	13.60	1.7
[0.97,0.98)	18.46	1.6	18.57	3.7
[0.98,0.99)	12.18	4.0	12.89	4.1
[0.99,1.00)	1.01	14.5	1.31	15.4

Table 9. Comparison of the nominal unfolded $(1/\sigma) d\sigma/dT$ and total fractional uncertainty with the published ALEPH 2004 result (HEPData ins:636645, Table 54) across the full measurement range ($0.55 \leq T < 1.0$). The ALEPH 2004 total uncertainty combines statistical, sys_1 , and sys_2 components in quadrature. Dashes indicate bins not covered by one or both measurements.

T range	$(1/\sigma) d\sigma/dT$		Stat. [%]		Exp. / Sys. 1 [%]		Theory / Sys. 2 [%]		Total [%]	
	Ours	ALEPH	Ours	ALEPH	Ours	ALEPH	Ours	ALEPH	Ours	ALEPH
[0.55,0.56)					—					
[0.56,0.57)	6.30×10^{-5}	—	88.8	—	467.8	—	67.7	—	500.9	—
[0.57,0.58)	1.22×10^{-3}	—	28.8	—	46.7	—	38.3	—	97.2	—
[0.58,0.59)	1.48×10^{-3}	1.15×10^{-3}	14.5	29.6	25.0	45.2	59.5	28.7	82.7	61.2
[0.59,0.60)	3.23×10^{-3}	2.29×10^{-3}	15.8	21.8	35.8	40.6	53.5	28.4	75.3	54.1
[0.60,0.61)	4.20×10^{-3}	3.50×10^{-3}	13.1	17.4	25.9	24.9	7.1	28.6	39.3	41.7
[0.61,0.62)	8.53×10^{-3}	8.39×10^{-3}	8.9	11.4	17.1	9.2	32.9	20.3	42.1	25.0
[0.62,0.63)	0.0131	0.0128	5.5	9.0	7.3	6.4	27.7	20.3	32.0	23.1
[0.63,0.64)	0.0248	0.0215	4.1	7.1	8.2	4.4	14.8	20.3	19.9	21.9
[0.64,0.65)	0.0411	0.0433	3.1	5.2	6.3	11.5	30.5	7.1	32.0	14.4
[0.65,0.66)	0.0695	0.0656	2.2	4.1	2.6	4.2	12.6	7.1	14.0	9.2
[0.66,0.67)	0.1068	0.1028	1.9	3.2	3.8	3.4	16.9	7.1	17.9	8.5
[0.67,0.68)	0.1305	0.1258	1.5	2.9	2.7	2.4	4.7	7.8	6.6	8.7
[0.68,0.69)	0.1587	0.1640	1.5	2.5	2.6	2.9	10.6	7.8	11.4	8.7
[0.69,0.70)	0.1776	0.1842	1.3	2.4	4.3	4.7	4.3	7.8	6.7	9.5
[0.70,0.71)	0.2087	0.2142	1.2	2.2	1.4	2.1	5.2	7.0	6.0	7.6
[0.71,0.72)	0.2448	0.2481	1.2	2.1	2.4	5.4	3.3	7.0	4.8	9.1
[0.72,0.73)	0.2876	0.2943	1.0	1.9	1.1	1.9	2.6	7.0	3.6	7.5
[0.73,0.74)	0.3210	0.3435	1.0	1.8	1.2	2.3	1.4	5.5	2.8	6.2
[0.74,0.75)	0.3792	0.3654	0.9	1.7	1.9	1.9	1.8	5.5	3.2	6.0
[0.75,0.76)	0.4332	0.4309	0.9	1.6	2.3	2.0	1.7	5.5	3.4	6.0
[0.76,0.77)	0.4958	0.4692	0.8	1.5	1.5	2.8	1.9	3.7	3.0	4.9
[0.77,0.78)	0.5504	0.5458	0.8	1.4	0.5	1.3	2.8	3.7	3.2	4.2
[0.78,0.79)	0.5994	0.5994	0.7	1.4	1.8	1.3	0.9	3.7	2.4	4.2
[0.79,0.80)	0.6550	0.6609	0.8	1.3	3.0	3.7	1.1	3.9	3.4	5.6
[0.80,0.81)	0.7399	0.7680	0.7	1.2	3.0	2.0	1.6	3.9	3.6	4.6
[0.81,0.82)	0.8395	0.8570	0.7	1.1	1.4	1.4	4.4	3.9	4.8	4.3
[0.82,0.83)	0.9697	0.9808	0.6	1.1	0.9	1.3	2.3	4.8	2.7	5.1
[0.83,0.84)	1.14	1.11	0.6	1.0	2.0	0.8	3.0	4.8	3.7	5.0
[0.84,0.85)	1.26	1.27	0.6	1.0	1.4	0.7	1.1	4.8	1.9	4.9
[0.85,0.86)	1.45	1.44	0.5	0.9	0.3	0.7	2.2	3.6	2.3	3.8
[0.86,0.87)	1.64	1.64	0.5	0.8	1.3	1.5	3.0	3.6	3.3	4.0
[0.87,0.88)	1.89	1.93	0.5	0.8	1.6	1.3	3.7	3.6	4.1	3.9
[0.88,0.89)	2.23	2.23	0.5	0.7	1.0	1.3	2.6	3.1	2.9	3.4
[0.89,0.90)	2.67	2.63	0.4	0.7	0.4	0.6	1.0	3.1	1.2	3.2
[0.90,0.91)	3.20	3.06	0.4	0.6	1.2	1.1	0.4	3.1	1.3	3.3
[0.91,0.92)	3.86	3.70	0.4	0.6	1.1	0.6	0.8	2.1	1.4	2.2
[0.92,0.93)	4.70	4.55	0.4	0.5	0.9	0.8	0.5	2.1	1.1	2.3
[0.93,0.94)	5.79	5.64	0.3	0.5	1.6	0.7	0.9	2.1	1.9	2.2
[0.94,0.95)	7.40	7.28	0.3	0.4	1.1	0.6	0.7	1.5	1.4	1.7
[0.95,0.96)	9.79	9.63	0.3	0.4	0.8	0.7	0.6	1.5	1.1	1.7
[0.96,0.97)	13.9	13.6	0.2	0.3	2.3	0.6	1.0	1.5	2.5	1.7
[0.97,0.98)	18.5	18.6	0.2	0.3	1.5	0.5	0.5	3.7	1.6	3.7
[0.98,0.99)	12.2	12.9	0.3	0.3	3.9	1.8	0.7	3.7	4.0	4.1
[0.99,1.00)	1.01	1.31	1.0	0.8	14.1	14.9	3.1	3.7	14.5	15.4

Table 10. Per-bin fractional uncertainty breakdown comparison between this analysis and the published ALEPH 2004 result (HEPData ins:636645, Table 54). For this analysis, Stat. is derived from the RooUnfold covariance, Exp. is the quadrature sum of all experimental track/event and neutral variations, and Theory is the max envelope of the three generator reweightings. For ALEPH 2004, Sys. 1 and Sys. 2 correspond to the two systematic components provided in the HEPData table. All values are absolute fractional uncertainties in percent; Total combines all components in quadrature. Dashes indicate bins outside the respective measurement range.

9.2 Per-source correlation matrices

The per-component correlation matrices are derived from the individual component covariance matrices $\text{Cov}_{ij}^{(c)}$ described in Sec. 8.6. For each component c , the correlation is

$$\rho_{ij}^{(c)} = \frac{\text{Cov}_{ij}^{(c)}}{\sqrt{\text{Cov}_{ii}^{(c)} \text{Cov}_{jj}^{(c)}}}. \quad (9.1)$$

Figure 21 shows all six components simultaneously, enabling direct comparison of their correlation structures.

The statistical component (top left) shows the narrow-band correlation pattern characteristic of IBU: neighboring bins are positively correlated through the unfolding propagation, but correlations fall off quickly with bin separation. The iteration component (top center) shows a similar but slightly broader structure, reflecting the coherent response of the unfolding regularization to low-frequency spectral features. The experimental component (top right) has a more extended positive-correlation band, driven by the coherent neutral-energy-response shifts (`nes_up`, `nes_down`) which move the thrust distribution in the same direction across a wide range of bins.

The theory component (bottom left) shows the strongest and most extended off-diagonal correlations of all six components. Generator-reweighting shifts are coherent across large thrust ranges because the parton-shower and hadronization changes affect the whole spectral shape rather than individual bins, making the theory covariance the dominant driver of off-diagonal structure in the total matrix. The hadronic correction (bottom center) shows modest correlations commensurate with its $\sim 3\%$ magnitude in the central range. The ISR correction (bottom right) is nearly diagonal, consistent with its sub-percent contribution and the bin-local nature of the MC-statistical uncertainty on the $C_{\text{ISR}}(j)$ ratio.

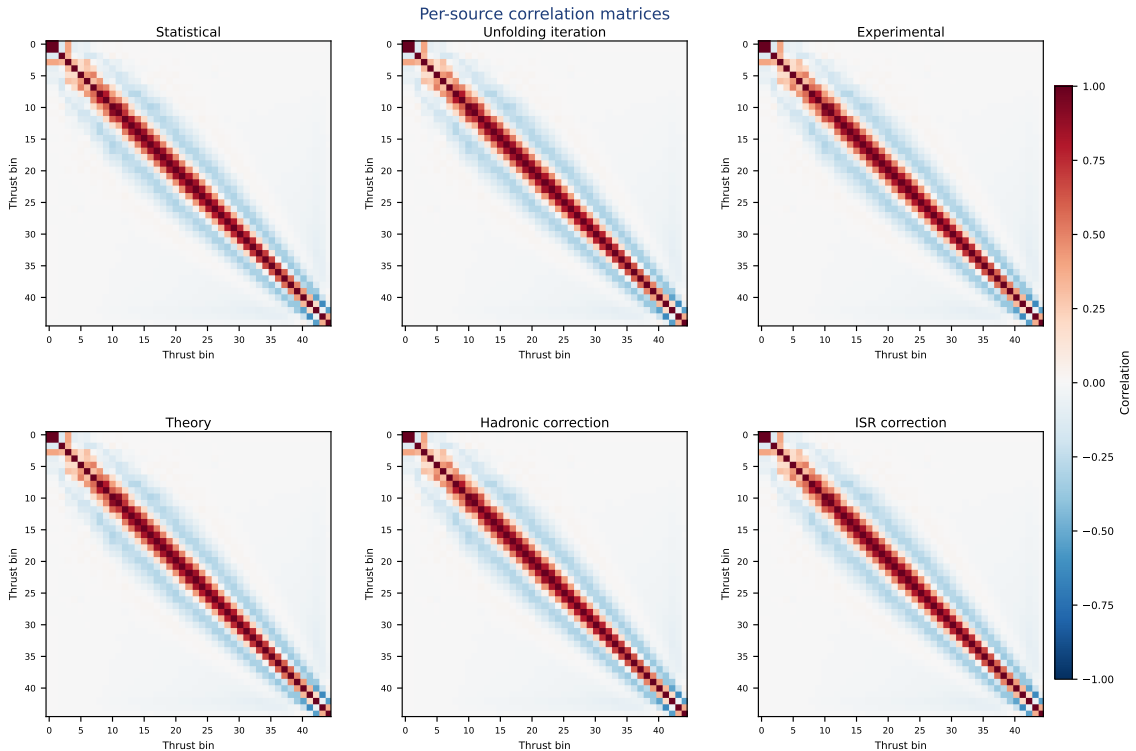


Figure 21. Per-source correlation matrices for the six independent uncertainty components: statistical (top left), unfolding-iteration (top center), experimental (top right), theory (bottom left), hadronic correction (bottom center), and ISR correction (bottom right). All matrices use the same color scale (-1 to $+1$, red/blue). The theory component shows the strongest and most extended off-diagonal structure, dominating the total correlation matrix.

9.3 Per-source covariance matrices

The covariance matrices encode both the per-bin uncertainty magnitudes and the bin-to-bin correlations for each source. The total covariance is the sum of all six component covariances:

$$\text{Cov}_{ij}^{(\text{tot})} = \text{Cov}_{ij}^{(\text{stat})} + \text{Cov}_{ij}^{(\text{iter})} + \text{Cov}_{ij}^{(\text{exp})} + \text{Cov}_{ij}^{(\text{theory})} + \text{Cov}_{ij}^{(\text{had})} + \text{Cov}_{ij}^{(\text{ISR})}. \quad (9.2)$$

Figure 22 shows the per-component covariance matrices; Fig. 23 shows the total.

The component covariance magnitudes directly reflect the per-bin uncertainty sizes shown in the breakdown plots of Sec. 8.8. The theory covariance (bottom left in Fig. 22) has the largest absolute values and the most extended off-diagonal structure, as expected from the dominant and spectrally coherent theory shifts. The experimental covariance has sub-leading magnitude but non-trivial off-diagonal entries driven by the coherent neutral-response variations. The statistical and iteration covariances are comparatively small; the ISR correction produces a near-diagonal covariance consistent with its bin-local MC-statistical origin.

The total covariance matrix (Fig. 23) is the primary product exported for theory use. Its off-diagonal structure is dominated by the theory covariance across the central thrust

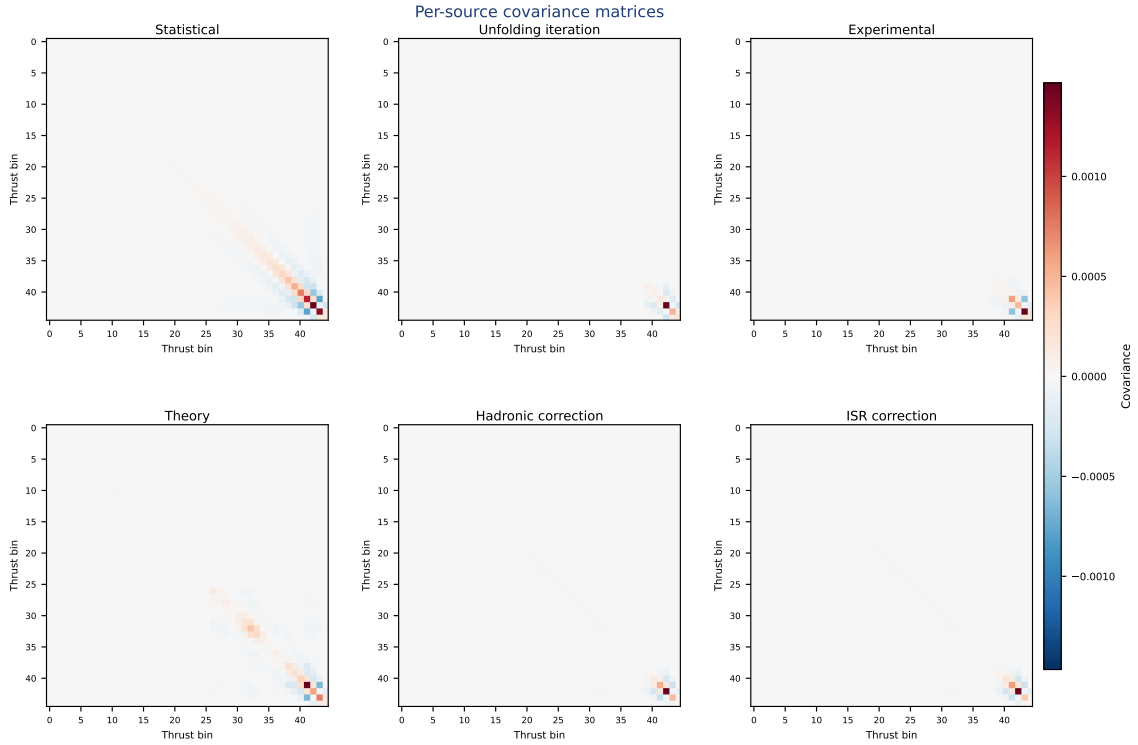


Figure 22. Per-source covariance matrices for the six independent uncertainty components: statistical (top left), unfolding-iteration (top center), experimental (top right), theory (bottom left), hadronic correction (bottom center), and ISR correction (bottom right). Each panel uses a symmetric color scale centered on zero (red: positive, blue: negative). The theory component dominates the total covariance in both magnitude and off-diagonal extent.

range, with additional contributions from the experimental component. Theory consumers are encouraged to use the fit-window total covariance (covering $0.505 \leq T < 1.00$, 45 bins) for α_s extractions rather than the full-range matrix, to avoid the regions of large uncertainty and poor MC-model control near the kinematic boundaries.

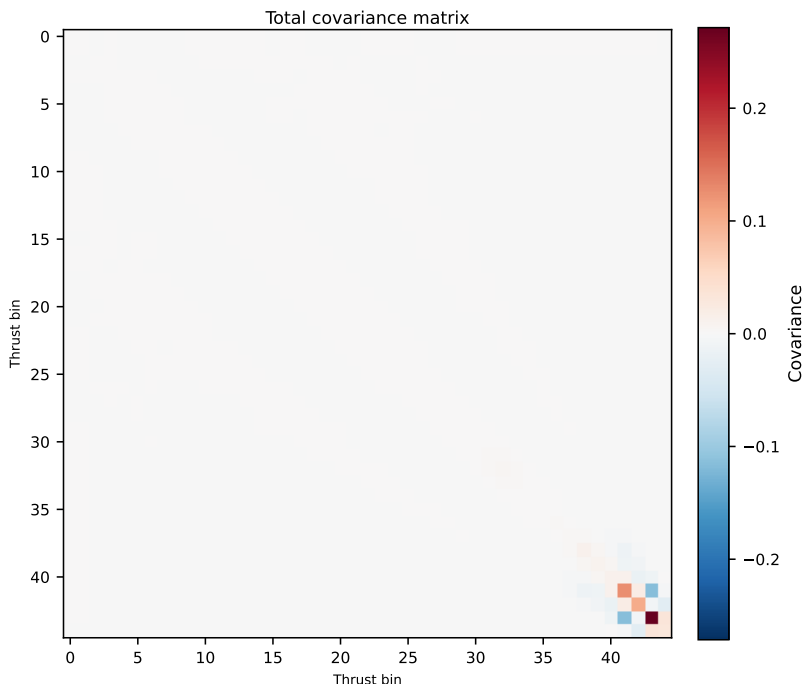


Figure 23. Total covariance matrix, combining all six uncertainty components. The off-diagonal structure is dominated by theory correlations across the central thrust range. The full covariance matrix must be used in any downstream fit; diagonal uncertainties alone would underestimate the true statistical power of the result. The fit-window version ($0.505 \leq T < 1.00$) is recommended for α_s extractions.

10 Conclusion

A complete thrust baseline measurement has been produced with Iterative Bayesian Unfolding on archived ALEPH 1994 data at $\sqrt{s} \simeq 91.2$ GeV. The analysis propagates six independent uncertainty components — statistical, unfolding regularization, experimental detector, theory modeling, hadronic event-selection correction, and ISR correction — and combines them in quadrature to form a full covariance matrix suitable for precision phenomenology. The implementation of the ISR correction, following the prescription of both published ALEPH event-shape analyses [12, 31], brings the measured thrust distribution into good agreement with the published ALEPH 2004 result ($\chi^2/\text{ndf} = 0.36$ over 42 bins), with the only notable discrepancy at the $T \rightarrow 1$ dijet endpoint where MC modeling uncertainties are largest and normalization conventions differ.

The precision QCD motivation for this work is the persistent e^+e^- α_s tension: recent thrust-based extractions yield $\alpha_s(m_Z) \simeq 0.1136$, approximately 3.5σ below the world average 0.1180 [20, 21]. The covariance and correlation products from this baseline are designed as direct inputs to precision α_s fits. The full-range and fit-window covariance matrices, central values, component-level uncertainty plots, and individual signed-shift branches are bundled as version-controlled release products, with provenance metadata recording the git commit, software versions, and key analysis parameters. Theory consumers are encouraged

to use the fit-window covariance products for extractions.

This establishes a first end-to-end repository baseline for thrust with IBU and defines the template for extension to C-parameter and heavy-jet mass, including future multidimensional correlation studies. The AI-agent operating model demonstrated in this cycle — executable-workflow orchestration under physicist supervision with full provenance tracking — provides a scalable framework for precision QCD as a testing ground for closed theory–experiment loops in fundamental physics.

11 Challenges with AI-agent analysis

This section is maintained as a living record of unresolved or recurring issues encountered during the analysis. Because this document is an internal note rather than a final publication, we prioritize explicit tracking of weaknesses, mitigation status, and open analysis challenges. Practical lessons from AI–physicist collaboration are discussed in Sec. 1.

11.1 Current limitations of the thrust-only baseline

The present release is robust enough for a preliminary thrust result, but several limitations remain:

- for events with exactly 3 selected particles, the thrust algorithm selects the highest-magnitude particle as the axis rather than enumerating all possible hemisphere assignments; this approximation is justified because (i) 3-particle hadronic events are rare in $Z \rightarrow q\bar{q}$ decays (impact on thrust value typically $\lesssim 0.1\%$ for $T > 0.5$), and (ii) the response-matrix migration structure dominates uncertainty in the endpoint bins where such events concentrate;
- hadronic-event correction uncertainty is propagated as an independent component (Δ_{had} , central-range mean $\approx 3.2\%$); the endpoint bins remain sensitive to correction-factor extrapolation;
- systematic inter-bin correlations use the statistical correlation matrix as a template ($\text{Cov}_{ij}^{(c)} = \Delta_c(i) \Delta_c(j) \rho_{ij}^{\text{stat}}$); this is an approximation that assumes systematic and statistical correlations share the same bin-to-bin structure;
- endpoint thrust bins remain statistically and modeling sensitive;
- analysis scope is currently one-dimensional (thrust only), while the future target includes the thrust-family observables and potentially multidimensional unfolding.

11.2 Persistent analysis challenges

Several recurrent issues have been tracked through the development of this note. Plot-style consistency across scripts has been an ongoing concern, with centralized style enforcement in producer scripts now largely resolving the issue. Method-to-code traceability gaps are addressed by the workflow and provenance tables in Sec. 7 and Sec. 9, with `workflow_summary.json` serving as the canonical numeric record. The most significant open challenge

is endpoint-bin instability: the final bin ($0.99 < T < 1.00$) is sensitive to MC modeling, hadronic correction extrapolation, and normalization convention differences, and dominates the maximum per-bin uncertainty. This is mitigated by reporting central-window metrics ($0.60 \leq T < 0.95$) alongside full-range figures throughout the note.

11.3 Update protocol for this section

For each major workflow iteration, this section should record:

- newly discovered persistent issues;
- whether previous issues moved from Open to In progress/Resolved;
- concrete next action and code location for unresolved items.

Keeping this log in the main body is intentional: it makes assumptions and remaining risks visible to internal readers and future maintainers.

11.4 Scaling human oversight: toward systematic validation

A recurring theme in this work is that the set of things that can go wrong silently grows rapidly with analysis complexity. The one-dimensional thrust measurement already required validation of event selection, unfolding closure, systematic propagation, covariance-matrix properties, and figure/table accuracy. Extending the program to additional observables, multidimensional unfolding, or theory–experiment feedback loops will multiply these failure modes.

The current mitigation relies on structured sign-off points, automated integrity checks (file presence, covariance positive semi-definiteness, fit-mask validity), and version-controlled provenance. While adequate for a single-observable proof of concept, this approach does not scale without further investment in systematic testing infrastructure.

Software engineering and machine-learning operations (MLOps) communities have partially addressed analogous challenges through continuous-integration and continuous-deployment (CI/CD) pipelines, where automated test suites run on every code change and failures block deployment. Adapting these patterns to physics analysis workflows is a natural next step: for example, automated regression tests could verify that modifying one systematic variation does not silently shift the unfolded spectrum outside a predefined tolerance. Physics-specific assertions — such as verifying that the unfolded distribution integrates to unity, that the response matrix is properly normalized, or that refolded spectra agree with detector-level data — could be encoded as unit tests that run after each agent iteration.

The key unsolved challenge is encoding implicit physics priors as testable assertions. Many of the validation checks performed by the physicist in this analysis (Sec. 3) rely on domain intuition that is difficult to formalize: recognizing that a φ excess indicates a detector artifact, judging whether a per-bin uncertainty is “physically reasonable,” or deciding that a 23% shift constitutes an observable redefinition rather than a systematic effect. Developing methods to translate such expert knowledge into machine-executable

tests — whether through formal specification languages, learned anomaly detectors, or structured physicist–agent dialogue protocols — is an important direction for making AI-assisted experimental physics robust and scalable.

Acknowledgments

The authors would like to thank Roberto Tenchini and Guenther Dissertori from the ALEPH Collaboration for their useful comments and suggestions on the use of ALEPH data. This work has been supported by Schmidt Sciences Foundation (to A.B.) and Department of Energy, Office of Science, under Grant No. DE-SC0011088 (to Y.-J.L.).

References

- [1] “The Electron-Positron Data Reanalysis Alliance.” <https://ee-alliance.org/home/>.
- [2] A. Badea, A. Baty, P. Chang, G.M. Innocenti, M. Maggi, C. Mcginn et al., *Measurements of two-particle correlations in e^+e^- collisions at 91 GeV with ALEPH archived data*, *Phys. Rev. Lett.* **123** (2019) 212002 [1906.00489].
- [3] Y. Chen et al., *Jet energy spectrum and substructure in e^+e^- collisions at 91.2 GeV with ALEPH Archived Data*, *JHEP* **06** (2022) 008 [2111.09914].
- [4] Y.-C. Chen, Y. Chen, A. Badea, A. Baty, G.M. Innocenti, M. Maggi et al., *Long-range near-side correlation in e^+e^- Collisions at 183–209 GeV with ALEPH Archived Data*, *Phys. Lett. B* **856** (2024) 138957 [2312.05084].
- [5] H. Bossi, Y. Chen, Y.-C. Chen, M. Jaarsma, Y. Li, J. Zhang et al., *Energy Correlators from Partons to Hadrons: Unveiling the Dynamics of the Strong Interactions with Archival ALEPH Data*, 2511.00149.
- [6] A. Badea, A. Baty, H. Bossi, Y.-C. Chen, Y. Chen, J. Zhang et al., *Unbinned measurement of thrust in e^+e^- collisions at $\sqrt{s} = 91.2$ GeV with ALEPH archived data*, 2510.22038.
- [7] Anthropic, “Accelerating Scientific Research.” <https://www.anthropic.com/news/accelerating-scientific-research>, 2025.
- [8] OpenAI, “Advancing Science and Math with GPT-5.2.” <https://openai.com/index/gpt-5-2-for-science-and-math/>, 2025.
- [9] G. DeepMind, “Gemini Deep Think: Accelerating Mathematical and Scientific Discovery.” <https://deepmind.google/blog/accelerating-mathematical-and-scientific-discovery-with-gemini-deep-think/>, 2025.
- [10] OpenAI, “GPT-5.2 Derives a New Result in Theoretical Physics.” <https://openai.com/index/new-result-theoretical-physics/>, 2026.
- [11] G. DeepMind, “AlphaProteo: Generating Novel Proteins for Biology and Health Research.” <https://deepmind.google/blog/alphaproteo-generates-novel-proteins-for-biology-and-health-research/>, 2025.
- [12] ALEPH collaboration, *Studies of QCD at e^+e^- centre-of-mass energies between 91-GeV and 209-GeV*, *Eur. Phys. J.* **C35** (2004) 457.

- [13] T.B. Brown et al., *Language Models are Few-Shot Learners*, *Adv. Neural Inf. Process. Syst.* **33** (2020) 1877 [[2005.14165](#)].
- [14] J. Wei et al., *Chain-of-thought prompting elicits reasoning in large language models*, *Adv. Neural Inf. Process. Syst.* **35** (2022) 24824 [[2201.11903](#)].
- [15] H. Wang, T. Fu, Y. Du et al., *Scientific discovery in the age of artificial intelligence*, *Nature* **620** (2023) 47.
- [16] L. Messeri and M.J. Crockett, *Artificial intelligence and illusions of understanding in scientific research*, *Nature* **627** (2024) 49.
- [17] D.P. Woodruff, V. Cohen-Addad, L. Jain et al., *Accelerating Scientific Research with Gemini: Case Studies and Common Techniques*, [2602.03837](#).
- [18] E. Farhi, *Quantum chromodynamics test for jets*, *Phys. Rev. Lett.* **39** (1977) 1587.
- [19] R. Abbate, M. Fickinger, A.H. Hoang, V. Mateu and I.W. Stewart, *Thrust at N^3LL with Power Corrections and a Precision Global Fit for $\alpha_s(m_Z)$* , *Phys. Rev. D* **83** (2011) 074021 [[1006.3080](#)].
- [20] M.A. Benitez, A.H. Hoang, V. Mateu, I.W. Stewart and G. Vita, *On Determining $\alpha_s(m_Z)$ from Dijets in e^+e^- Thrust*, [2412.15164](#).
- [21] PARTICLE DATA GROUP collaboration, *Review of Particle Physics*, *PTEP* **2022** (2022) 083C01.
- [22] M. Abolhasani and E. Kumacheva, *The rise of self-driving labs in chemical and materials sciences*, *Nature Synthesis* **2** (2023) 483.
- [23] B.P. MacLeod, F.G.L. Parlane, T.D. Morrissey, F. Hase, L.M. Roch, C.P. Berlinguette et al., *Self-driving laboratory for accelerated discovery of thin-film materials*, *Sci. Adv.* **6** (2020) eaaz8867.
- [24] Y. Chen, C. Li, Z. Gou et al., *ScienceAgentBench: Toward Rigorous Assessment of Language Agents for Data-Driven Scientific Discovery*, [2410.05080](#).
- [25] C. Lu, C. Lu, R. Lange, J. Foerster, J. Clune and D. Ha, *The AI Scientist: Towards Fully Automated Open-Ended Scientific Discovery*, [2408.06292](#).
- [26] S. Bubeck, C. Coester, R. Eldan, T. Gowers, Y.T. Lee, A. Lupsasca et al., *Early science acceleration experiments with GPT-5*, [2511.16072](#).
- [27] A. Guevara, A. Lupsasca, D. Skinner, A. Strominger and K. Weil, *Single-minus gluon tree amplitudes are nonzero*, [2602.12176](#).
- [28] M.D. Schwartz, *Resummation of the C-Parameter Sudakov Shoulder Using Effective Field Theory*, [2601.02484](#).
- [29] ALEPH collaboration, *ALEPH: A detector for electron-positron annihilations at LEP*, *Nucl. Instrum. Meth.* **A294** (1990) 121.
- [30] ALEPH collaboration, *Performance of the ALEPH detector at LEP*, *Nucl. Instrum. Meth. A* **360** (1995) 481.
- [31] ALEPH collaboration, *Studies of quantum chromodynamics with the ALEPH detector*, *Phys. Rept.* **294** (1998) 1.

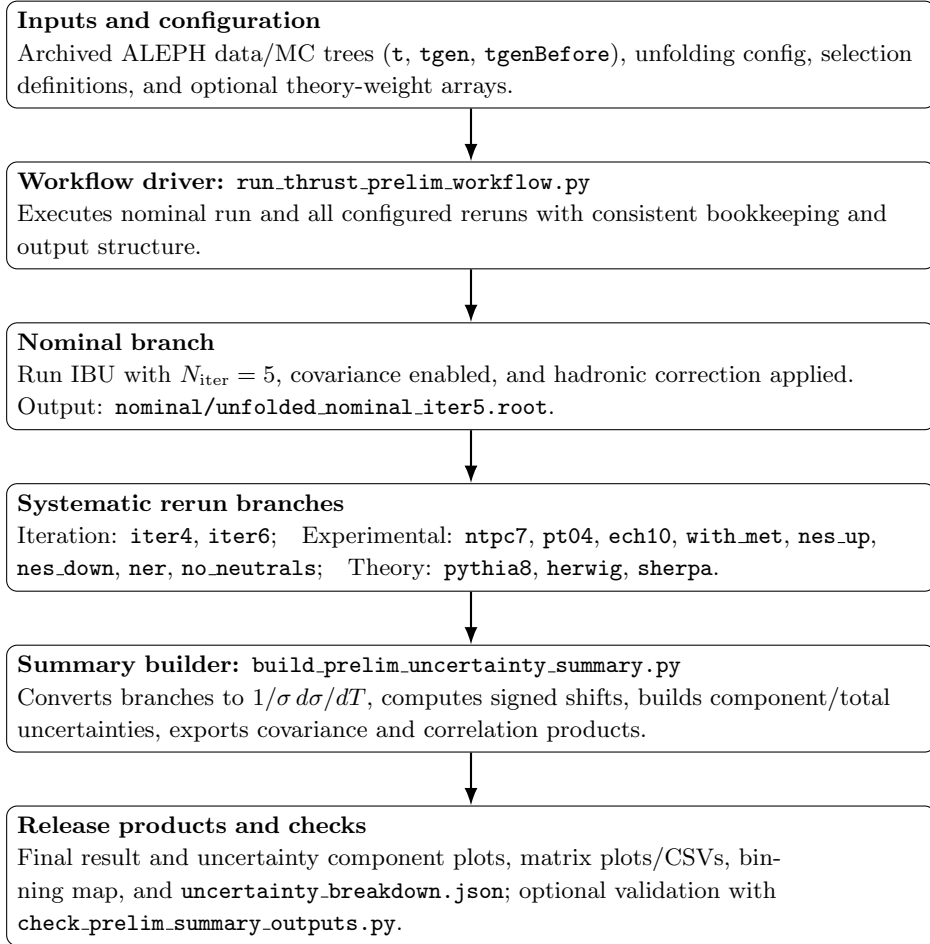


Figure 24. Schematic analysis flow for the thrust preliminary workflow. This replaces the dense workflow table and shows the execution order and branch structure used in this internal note.

A Workflow code and reproduction contract

This appendix documents the executable workflow structure, command sequences, and pseudocode for the thrust analysis, moved here from the main text to keep the analysis sections focused on physics content.

A.1 Executable workflow map

The thrust preliminary workflow uses two entrypoints (both under `Unfolding/scripts/`):

- `run_thrust_prelim_workflow.py` for nominal and systematic reruns;
- `build_prelim_uncertainty_summary.py` for uncertainty assembly and final summaries.

Figure 24 summarizes the executable stages and branch structure.

A.2 Reproduction contract

The following command sequence is the explicit rerun contract for this note. It assumes a ROOT-enabled Python environment and shell access to ROOT libraries.

```
# Example environment setup
source ~/code/root/bin/thisroot.sh
conda activate py312
RUN_DIR=Studies/PreliminaryResult/2026-02-17_thrust_iter5
NOM_ROOT=$RUN_DIR/nominal/unfolded_nominal_iter5.root
SUM_DIR=$RUN_DIR/summary
MATRIX_SCRIPT=Studies/UnfoldingIterationScan/scripts/make_unfolding_matrix_plots.py

# 1) Full workflow (nominal + iteration + experimental + theory)
python Unfolding/scripts/run_thrust_prelim_workflow.py \
  --config Unfolding/unfold_config.json \
  --outdir $RUN_DIR \
  --nominal-iter 5 --iter-down 4 --iter-up 6 \
  --theory-weights-dir /path/to/theory_reweighting/training-<tag>

# 2) Uncertainty summary and final result plots
python Unfolding/scripts/build_prelim_uncertainty_summary.py \
  --base-dir $RUN_DIR \
  --outdir $SUM_DIR \
  --aleph-csv /path/to/HEPData-ins636645-v1-Table_54.csv

# 3) Matrix plots and CSV exports
python $MATRIX_SCRIPT \
  --input-root $NOM_ROOT \
  --outdir $SUM_DIR/matrices_nominal_iter5

# 4) Output integrity check
python Unfolding/scripts/check_prelim_summary_outputs.py \
  --base-dir $RUN_DIR
```

The `--theory-weights-dir` argument is required unless theory variations are explicitly skipped. If the ALEPH CSV is not available at the repository-local default location, `--aleph-csv` must be provided explicitly.

A.3 Workflow pseudocode

Nominal and systematics execution logic is summarized below.

```
load nominal configuration
run nominal unfolding (iterations=5, covariance=true)
```

```

run iteration variations (iterations=4,6)
run experimental variations (ntpc7, pt04, ech10, with_met,
                             nes_up, nes_down, ner, no_neutrals)
run theory variations with event-level weights (pythia8, herwig, sherpa)
build uncertainty summary products and final plots
export covariance/correlation CSVs and matrix visualizations
validate required outputs and consistency checks

```

Uncertainty-summary logic:

```

convert all unfolded branches to 1/sigma dsigma/dT
compute signed branch shifts delta_v = (U_v - U_nom)/U_nom
build components:
  iteration = envelope(iter4, iter6)
  track/event = quadrature(ntpc7, pt04, ech10, with_met)
  neutral = quadrature(envelope(nes_up, nes_down), ner)
  theory = envelope(pythia8, herwig, sherpa)
  hadronic = envelope(up/down C_had uncertainty)
build component covariance model (nominal: template_correlated)
combine total = stat + iteration + experimental + theory + hadronic
write component plots and final comparison plot
write full-range and fit-window covariance/correlation outputs

```

B Validation and cross-check details

This appendix collects supplementary validation material that supports the analysis decisions described in the main text.

B.1 Iteration-scan closure and stability

The iteration-scan diagnostics used to select $N_{\text{iter}} = 5$ confirm that the refolded spectra reproduce the detector-level data shape within the expected level of statistical fluctuation. The closure-shape χ^2/ndf is stable across $N_{\text{iter}} \in \{4, 5, 6\}$, and the iteration-to-iteration shift in the unfolded spectrum decreases monotonically before flattening near $N_{\text{iter}} = 5$ –6, consistent with convergence. The $N_{\text{iter}} = 100$ refolding confirms that the response model does not diverge at high iteration, though the unfolded spectrum in that limit becomes increasingly sensitive to statistical fluctuations.

B.2 OmniFold and prior IBU comparison

The comparison with OmniFold and prior Iterative Bayesian Unfolding spectra from `unfold-ee-logtau/Resu` is documented in Sec. 9 (Fig. 19). Compatibility metrics are $\chi^2/\text{ndf} = 0.663$ (OmniFold), 0.421 (prior IBU), evaluated over the 42 ALEPH bins using the current total uncertainty model on the diagonal. Differences are localized to the high-thrust endpoint and are consistent with the expected sensitivity of IBU to regularization strength and normalization convention in that region.

B.3 Difference-check program

A structured diagnostic program for inter-analysis differences (binning/normalization alignment, hadronic-correction treatment, event/sample synchronization, regularization dependence, and theory-envelope masking) is documented in `Plans/2026-02-19_thrust_difference_checks.md`. Execution and acceptance criteria are defined there; no final physics interpretation of residual inter-analysis differences is assigned until that program is completed.

B.4 Output integrity verification

After each full workflow run, a dedicated script `check_prelim_summary_outputs.py` verifies that all required output files are present and non-empty, that the covariance matrix is positive semi-definite on the diagonal, and that the fit mask selects a non-zero number of bins. The 2026-03-05 run passed all checks (1/1 integrity check passed).

C Communication summary (reconstructed project-cycle transcript)

This appendix records a reconstructed full communication summary for the current thrust-analysis cycle. The source material is the project artifact trail (plans, note rewrites, workflow outputs, and validation products), not a verbatim message log. The objective is to preserve the decision chain for internal reproducibility and method auditing.

C.1 Scope and reconstruction sources

Scope covered: the thrust Iterative Bayesian Unfolding cycle from code review through preliminary-result packaging and note rewrites (Sections 1–8), including the AI-agent collaboration framing.

Primary reconstruction sources:

- dated planning artifacts under `Plans/` (2026-02-13 to 2026-02-18);
- executable workflow outputs in `Studies/PreliminaryResult/`, with run directory `2026-03-05_thrust_iter5/`;
- note section revision trail in `AnalysisNote/sections/*.tex`;
- workflow scripts in `Unfolding/scripts/` and `Studies/*/scripts/`.

C.2 Reconstructed communication timeline

1. **Initial objective setting (2026-02-13).** The collaboration established a thrust-first execution strategy with Iterative Bayesian Unfolding, complete code review, and a JHEP-style internal-note structure.
2. **Code-audit phase.** Critical and high-impact defects were identified and fixed (tree defaults, closure mode requirements, return-code handling, systematics path robustness), with findings tracked in `Plans/2026-02-13_code_review_findings.md`.

3. **1994 workflow focus.** Execution direction was corrected to run the full 1994 derivation and unfolding chain rather than legacy partial-year paths.
4. **Nominal-regularization policy convergence.** The cycle converged on nominal $N_{\text{iter}} = 5$ with 4/6 as regularization systematic envelope for this thrust preliminary pass.
5. **Systematics completion requirement.** The scope was expanded to include full experimental and theory branches in the same run-owned output package, with hadronic correction retained in nominal processing.
6. **Result-style iteration loop.** Multiple rounds of visual QA enforced consistent pad geometry, ratio-panel readability, uncertainty normalization conventions, and legend/text placement for publication-grade interpretation.
7. **ALEPH comparison integration.** Final-result plotting was upgraded to include ratio to ALEPH 2004 in matched binning with uncertainty propagation via ROOT histogram operations.
8. **Uncertainty decomposition policy.** The workflow migrated from envelope-only views to explicit component-level plots, including signed shifts, grouped uncertainty structure, and central-window interpretation.
9. **Section-by-section rewrite cycle (Sections 1–5 first).** The note was expanded with stronger physics motivation, detector/data context, and reconstruction validation text connected directly to thrust sensitivity.
10. **Sections 5+ hardening.** Methods, systematics, and results sections were restructured for executable traceability (script entrypoints, output paths, and release artifacts).
11. **AI-agent narrative formalization.** A dedicated section captured operating model, controls, and measurable scorecard, followed by a final chapter logging persistent collaboration and analysis challenges.
12. **Physics-tone refinement.** Introductory framing was strengthened around precision-QCD motivation, LEP data quality, and validation goals.
13. **External-citation expansion.** AI-for-science and agent-workflow references were expanded, then extended with requested recent case studies.
14. **Reproducibility emphasis.** The communication repeatedly enforced path-level provenance for figures and summary products, with explicit checks and output validation scripts.

15. **Current-cycle layout request.** Results narrative was requested to present uncertainty decomposition before the final unfolded comparison, and to add a final-result total correlation matrix view.
16. **Current-cycle documentation request.** A complete communication appendix was requested for community context, with highlighted key decisions and rationale.

C.3 Key exchanges and decisions

<p>Decision: Use Iterative Bayesian Unfolding as the baseline correction method for this cycle.</p> <p>Rationale: Fast iteration without model retraining was required for rapid experimental cross-check loops.</p> <p>Impact: Workflow scripts, method text, and uncertainty propagation were all aligned to IBU.</p>
<p>Decision: Set nominal regularization to $N_{\text{iter}} = 5$ with 4/6 as regularization systematic.</p> <p>Rationale: Iteration-scan diagnostics and practical stability/throughput tradeoffs favored this operating point.</p> <p>Impact: All nominal and systematic branches, note text, and final plots were normalized to the same policy.</p>
<p>Decision: Run the full 1994 chain as the maintained baseline dataset year.</p> <p>Rationale: The analysis state required consistency in data/MC derivation and response inputs for one complete production year.</p> <p>Impact: Output provenance and note references were consolidated under run-owned 1994 directories.</p>
<p>Decision: Adopt a strict figure-style contract for result plots (connected pads, controlled ratio range, readable labels).</p> <p>Rationale: Visual interpretation quality was treated as analysis-relevant, not cosmetic.</p> <p>Impact: Several plotting scripts were iteratively corrected until style and uncertainty semantics stabilized.</p>
<p>Decision: Promote component-level uncertainty views (statistical, unfolding, experimental, theory) over envelope-only summaries.</p> <p>Rationale: Readers need source-resolved behavior rather than only combined envelopes.</p> <p>Impact: Results section now reports component behavior explicitly and ties interpretation to central-window metrics.</p>
<p>Decision: Keep “no-neutrals” as a cross-check branch and separate it from nominal total uncertainty.</p> <p>Rationale: It is a stress test rather than a baseline uncertainty source.</p> <p>Impact: Cross-check visibility is preserved while nominal total remains policy-consistent.</p>

<p>Decision: Introduce explicit AI-agent operating-model and challenge-tracking sections.</p> <p>Rationale: The internal-note objective includes evaluating whether an agent can execute research workflows under supervision.</p> <p>Impact: The note now contains controls, measurable scorecard, and persistent challenge logging.</p>
<p>Decision: Expand citations to include recent AI+scientist and theory-assistant case studies.</p> <p>Rationale: Program motivation required concrete external evidence beyond generic AI discussion.</p> <p>Impact: Introduction and AI-agent sections now cite both broad and recent workflow-relevant studies.</p>
<p>Decision: Reorder results narrative to show uncertainty structure before final unfolded comparison.</p> <p>Rationale: Interpretation of the final spectrum is clearer once uncertainty sources are established first.</p> <p>Impact: Section flow now progresses from component structure to correlated final products to central comparison.</p>
<p>Decision: Add a final-result total correlation matrix plot from <code>corr_total.csv</code>.</p> <p>Rationale: Community-facing usage requires direct visibility of correlated uncertainties after full nominal combination.</p> <p>Impact: Release package now includes a dedicated final total-correlation figure and script-level provenance.</p>

C.4 Communication-pattern summary

The reconstructed cycle indicates a high-frequency specification–execution loop with strong emphasis on:

- explicit physics-policy locking before broader text expansion;
- figure-level interpretability as a first-class requirement;
- command/path-level provenance for every released artifact;
- incremental correction and revalidation rather than large unreviewed batches.

The dominant friction points were precision formatting constraints, rapid scope evolution, and synchronization between code outputs and note narrative. These patterns are consistent with the persistent-challenge tracker in Sec. 11.